

THAT LOOKS ABOUT RIGHT!



**UNIVERSITY OF CALIFORNIA
SAN DIEGO**

2020-2021

**AIAA DESIGN, BUILD, FLY
DESIGN REPORT**

TABLE OF CONTENTS

§	1	Executive summary	3	page
§	2	Management summary	4	page
<hr/>				
		2.1 :: Team organization and personnel	4	
<hr/>				
		2.2 :: Project timeline	5	
§	3	Conceptual design	7	page
<hr/>				
		3.1 :: Competition overview	7	
<hr/>				
		3.2 :: Scoring study	10	
<hr/>				
		3.3 :: Translation into design requirements	12	
<hr/>				
		3.4 :: Configuration selection	12	
<hr/>				
		3.5 :: Final conceptual design	18	
§	4	Preliminary design	19	page
<hr/>				
		4.1 :: Overall design methodology	19	
<hr/>				
		4.2 :: Design trade studies	19	
<hr/>				
		4.3 :: Aerodynamic analyses	20	
<hr/>				
		4.4 :: Stability and control analyses	24	
<hr/>				
		4.5 :: Mission model	25	
<hr/>				



TABLE OF CONTENTS (CONTINUED)

§	page	
5	Detail design	27
	5.1 :: Final design parameters	27
	5.2 :: Structural characteristics and capabilities	28
	5.3 :: System and subsystem architecture	29
	5.4 :: Weight and balance	36
	5.5 :: Expected performance	37
	5.6 :: Drawing package	37
6	Manufacturing plan	38
	6.1 :: Investigation of manufacturing processes	38
	6.2 :: Assembly method selection	38
	6.3 :: Manufacturing timeline	40
7	Testing plan	41
	7.1 :: Aircraft and subsystem testing plan	41
	7.2 :: Flight testing plan	42
8	Performance results	44
	8.1 :: Aircraft and subsystem performance	44
	8.2 :: Flight performance	46
9	Bibliography	49





§ 1

Executive summary

This design report, prepared by the DBF team at the University of California, San Diego, extensively describes the design, manufacturing, and testing processes it has adopted to develop an unmanned, remote-controlled aircraft capable of delivering shipment containers, towing a sensor, and achieving other tasks required to succeed in the 2020-21 AIAA DBF fly-off's four missions.

Design process :: UCSD DBF's conceptual design decisions emphasize the plane's ability to tow a long sensor, based on the importance of this technical property during the third-mission, and accommodate many containers, based on the scoring requirements of the shipment and surveillance flights (§ 3.1-3.2). These points of emphasis can be resolved by designing an efficient deployment mechanism and sizing the fuselage and lifting surfaces appropriately. In accordance with these considerations, the team has opted to build a T-tail dual-motor monoplane with a rectangular wing, square fuselage, and tricycle landing gear (§ 3.3).

During preliminary design, the team used force analyses and design trades to choose from a multitude of propulsion and aerodynamic configurations (§ 4.1-4.4). In the detail design phase, the team considered the structural makeup of the empennage, fuselage, and wing based on the aircraft's finalized dimensions and balance. This phase also accounts for the design of the plane's sub-systems, such as its loading mechanisms and higher-voltage avionics— noteworthy as a remedy to a critical issue experienced by the 2018-19 team's competition aircraft (§ 5.3). These preliminary and detail design decisions form the basis for the provided flight (§ 5.5) and mission (§ 5.6) performance estimations.

Final capabilities :: Based on data collected during completed test flights (§ 7-8), the 2020-2021 UCSD DBF competition prototype can

- complete one lap in 22 s. unloaded (31 s. when loaded);
- endure a flight of 14 *min.* at cruising speed;
- accommodate ten 30 *in.* long containers, for a maximum gross weight of 16 *lb.*; and
- complete a maximum of 21 laps while towing the sensor.

The remaining sections of this report discuss UCSD DBF's hierarchical structure (§ 2.1), the impact of the COVID-19 pandemic on its project schedule (§ 2.2), fabrication plan (§ 6), and its testing process (§ 7-8).



2 Management summary

The following section details UCSD DBF's organization and outlines the team's project timeline. It also discusses in detail the impact that the COVID-19 pandemic has had on their schedule.

2.1 - Team organization and personnel :: UCSD DBF follows a functional team structure, organizing members and assigning duties for action items in the most effective manner. A project manager and chief engineer leads six subteams divided by engineering discipline. A faculty advisor and members from prior seasons also counsel the team. **Figure 2.1.a** outlines the hierarchical organization between the team's alumni, faculty advisor, and current members.

Each week, the project manager and chief engineer preside over a meeting with subteam leaders. In these meetings, they discuss the achievement of milestones, progress on important tasks, and-- with the approval of both managers and a consensus of the attendees-- make the team's decisions.



Figure 2.1.a - UCSD DBF team structure.

The subteam disciplines that make up the team include aerodynamics, fabrication, finance, propulsion, report, and structures. **Table 2.1.1** describes the responsibilities and general tasks designated to each subteam. Non-lead members may choose to participate in more than one subteam; they are, however, encouraged to specialize in the operations of one specific subteam. This structure ensures that these members are sufficiently cross-trained and have enough expertise to succeed outgoing members.

Subteam	Function
Aerodynamics	Designs control surfaces, selects airfoils, and sizes wing and tail to minimize drag.
Fabrication	Builds and assembles aircraft components; defines manufacturing limitations.
Finance	Handles purchases and expenses, networks with industry, and secures funds.
Propulsion	Conducts thrust stand tests; sizes motor, propeller, and battery to optimize thrust.
Report	Communicates competition rules; writes and edits proposals and reports.
Structures	Conducts structural analyses and integrity tests; designs aircraft components.

Table 2.1.2 - List of the six subteams and their responsibilities.

2.2.- Project timeline :: UCSD DBF prepared a timeline for the 2020-2021 competition season, shown in **Figure 2.2.a**, which includes the deadlines of the team's four major objectives. The Gantt chart tracks the progress of the design, analysis, fabrication, and testing of the team's aircraft and its subsystems. They plan to work on each component in the weeks emphasized on the chart in blue; the team's actual timeline is shown in gold. They considered fabrication task items complete once integrated into the aircraft.

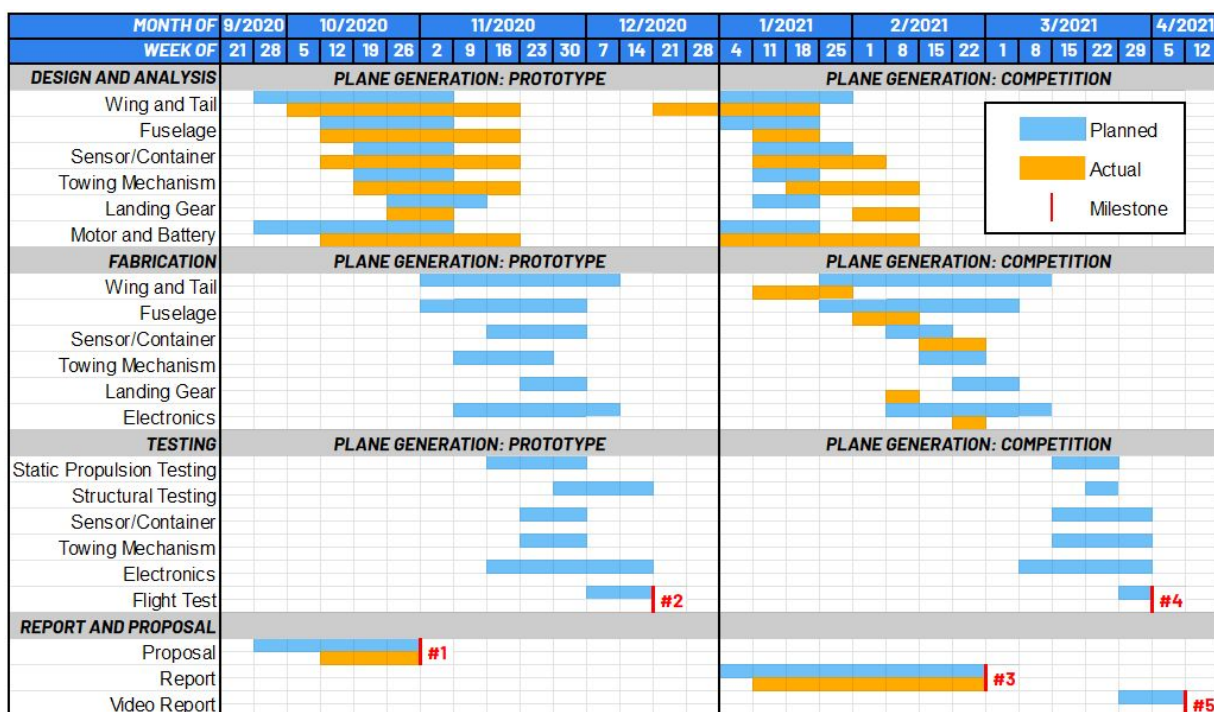


Figure 2.2.a · Project timeline (Gantt chart) for the 2020-2021 competition season.

The red bars on the timeline represent the weeks when a milestone occurs. These dates are submission deadlines, according to competition requirements, or self-imposed deadlines by which the team aimed to create a flight-worthy aircraft. **Table 2.2.1** lists these milestones, their deadlines, and completion status.

Milestone	Deadline	Completion	Status
1. Proposal submission	31 October 2020	30 October 2020	✓
2. Prototype plane completion	11 December 2020		X
3. Report submission	19 February 2021	18 February 2021	✓
4. Competition plane completion	2 April 2021		WIP
5. Video submission	18 April 2021		WIP

Table 2.2.1 · List of the team's milestones, their deadlines, and dates of completion. For tasks in progress, the estimated date of completion is listed.



Impact of COVID-19 on project timeline :: In response to the COVID-19 pandemic, the University of California, San Diego began in March 2020 facilitating most activities, including many classes and student organizations, to remote, online platforms. Following state and local guidelines, the university restricted access to non-residential buildings, including the team's workshop. All team members have committed to physical distancing practices in their capacities as UCSD DBF affiliates until state, local, and university authorities approve non-essential congregation. These actions, however, have significantly impacted the team's initial project timeline and milestone achievement plans.

The pandemic limited team members' access to hardware, materials, and tools for much of the 2020-21 season. Thus, the team could not fabricate a preliminary prototype aircraft; consequently, they abandoned their plans to do so. While **Table 2.2.1** indicates the team's inability to complete the milestone, they still developed a conceptual and preliminary design for the prototype.

In early January 2021, the university granted the team conditional, limited-time access to their on-campus workshop and allowed them to retrieve various hardware, parts, and tools. As part of this agreement, the team designated one member to retrieve, utilize, and assemble these items, ensuring that they'd continue to follow appropriate physical distancing measures throughout the retrieval and fabrication process.

This agreement allowed the team member to fabricate and assemble an aircraft that would serve as both a prototype and a competition plane. Because the responsibility of fabrication and testing lay solely on that member, the team placed significant consideration on its ease of manufacturability and repairability during their design decisions; this is reflected in the configuration selection (discussed in § 3.4). While, as shown in **Figure 2.2.a**, it is not yet in its final configuration and its expected completion is in April 2021, the team has used the aircraft as a testing prototype.

On 22 January 2021, the Design, Build, Fly organizing committee canceled the in-person fly-off, initially scheduled between 15-18 April 2021 in Tucson, Arizona. Teams will instead submit a pre-recorded flight video to a virtual contest that the committee plans to host on the same weekend. As demonstrated in **Figure 2.2.a** and **Table 2.2.1**, the team intends to submit a media presentation by this deadline.





3

Conceptual design

In the first stage of design, UCSD DBF analyzed competition guidelines, mission requirements, safety regulations, and scoring methodology to establish their contest goals. The team also examined several aircraft configurations to develop a realistic prototype-- deliverable within the project timeline. This section extensively discusses their process.

3.1 - Competition overview :: During the fly-off, teams will complete three flight missions and one ground-mission. In conjunction with the score of this design report, the results of these missions comprise the team's total score, as shown in **Equation 3.1**. The team's design decisions are chiefly motivated by the scoring methodology for each mission.

$$Sc_{TOT} == Sc_{REP} (Sc_{GM} + Sc_{M1} + Sc_{M2} + Sc_{M3}) \quad \text{Equation 3.1}$$

Ground-mission :: Before flying, teams will participate in a timed demonstration of their aircraft's system and subsystem operations. In this ground-mission, the team's designated assembly crewmember will load the containers and the deployment mechanism onto the aircraft while their pilot will prove that its flight controls operate nominally. UCSD DBF's completion time, normalized by that of the fly-off's fastest team, constitutes their ground-mission score (**Equation 3.2**).

The team will be eligible to fly in subsequent flight missions upon their successful completion of the ground-mission.

$$Sc_{GM} == \frac{T_{fastest}}{T_{UCSD}} \quad \text{Equation 3.2}$$

Flight path :: For each flight mission, aircraft must follow a path that the contest guidelines defined. As depicted in **Figure 3.1.a**, the route resembles a modified oval track and consists of 1,000 ft. straights-- represented by the figure's blue segments-- connected at its ends by two 180° turns, shown in green. In the middle of the downwind straight, the aircraft must also complete a 360° turn, shown in yellow.

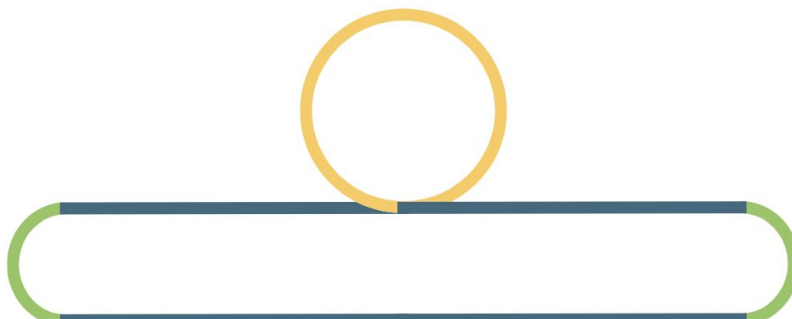


Figure 3.1.a - Aerial view of the AIAA DBF competition flight path.



Henceforth, a "lap" refers to the aircraft's completion of a circuit around this course, finishing in the air directly over the starting line.

Flight missions :: After completing the ground-mission, teams will demonstrate their aircraft's flight capability. During the first flight mission, the unloaded aircraft must abide by the general flight path requirements and land after finishing three laps within 5 *min.* of takeoff. The team is rewarded one point upon successful landing (**Equation 3.3**) and becomes eligible to fly in the next mission.

$$Sc_{M1} == 1.0$$

Equation 3.3

For the second flight, teams will simulate a shipment mission. While bearing containers-- each of equal size and weight-- and the sensor's deployment mechanism as payload, aircraft must land successfully after finishing three laps within 5 *min.* of takeoff, though faster completion times will benefit teams. Their total payload size cannot exceed the size they declare during technical inspection.

The ratio between the aircraft's container count and its completion time, normalized by the highest such ratio achieved in the fly-off, determines the team's second-mission score (**Equation 3.4**). Upon successful landing, the team becomes eligible to participate in the next mission.

$$Sc_{M2} == 1.0 + \frac{(nC/T)_{UCSD}}{(nC/T)_{MAX}}$$

Equation 3.4

During the final flight, teams will simulate a surveillance mission. While completing as many laps as possible within 10 *min.*, the aircraft must carry the sensor and its deployment mechanism. Teams must show their ability to deploy, operate, and retrieve the sensor remotely. Between the first and final 360° turns, the aircraft must tow the initially-stowed sensor; upon landing, the latter must be fully retracted.

The product of the sensor's length, weight, and the aircraft's completed number of laps, normalized by the highest such factor achieved in the fly-off, comprise the team's third-mission score (**Equation 3.5**).

$$Sc_{M3} == 2.0 + \frac{(nL \times L_{SEN} \times W_{SEN})_{UCSD}}{(nL \times L_{SEN} \times W_{SEN})_{MAX}}$$

Equation 3.5

By successfully completing each mission, the team will attain a score between [4, 7]. Subsequent scoring studies assumed that the team accomplishes such a task.

Design constraints :: The contest guidelines define several design constraints, listed in **Table 3.1.1**.

Category	Constraints
General	<ul style="list-style-type: none"> - Maximum allowable wingspan is 5 ft. - Second payload transmitter may be used for deployment, operation, and recovery of the towed sensor only.
Sensor	<ul style="list-style-type: none"> - Have a minimum diameter of 1 in. with a minimum fineness ratio of 4. - Be aerodynamically stable while deploying, operating and recovering the sensor. The aircraft cannot spin or rotate.
Sensor functionality	<ul style="list-style-type: none"> - Have a minimum of 3 external lights that can be viewed while in flight in the deployed position. - Lights are operated one at a time in the deployed position in a pattern to be determined by the team. - Lights are visible by the Flight Director. - Lights to be turned on and off remotely via the flight or payload transmitter. - Lights are controlled by a physical connection to the via the tow cable. - Contains its own battery power supply compliant with the battery requirements herein. - Carried internally to the airplane with no part of the sensor being part of or extruded outside of the airplane external surfaces or features.
Deployment and recovery mechanism	<ul style="list-style-type: none"> - Not required on all missions, but any pylons, covers or fairing required for the mechanism must be included in all missions. - Carried on Mission 2, but does not have to be in the Mission 3 location or configuration. - Deploys the sensor a minimum of 10X the total length of the sensor from the exit location of the airplane. - Tether includes a marker such that the Flight Line Director can verify it is fully deployed in flight.
Container	<ul style="list-style-type: none"> - Fully encloses the sensor and protects it from drop shock events. - Container simulators must be the same size (+/- 1/8 inch) and weight (or greater) and weight as the sensor shipping container with sensor. - Protect the sensor from damage during drop testing in the Ground Mission.
Power supply	<ul style="list-style-type: none"> - All power for takeoff and flight will be sourced from the aircraft's propulsion system. - Use of unaltered and commercially-produced lithium polymer (LiPo), nickel cadmium (NiCad), or nickel metal hydride batteries (NiMH). - If more than one battery pack is implemented, all commercial battery packs must be identical.

Table 3.1.1 · List of significant design constraints.



3.2 - Scoring study :: To inform their design process and better understand the competition's ruleset, UCSD DBF conducted a sensitivity study. While creating a baseline model, the team considered several assumptions and design constraints to derive simple governing equations. The model neglected differences between the sensor's geometric and material properties to confine the analysis to the sensor's length. With these assumptions, the team analyzed the tradeoffs between increasing its radius or length.

As the third-mission score is proportionally related to the sensor's length, the model assumed the sensor's diameter is 1 *in.*-- allowing a maximum aspect ratio without compromising the sensor's ability to carry its electronic components.

The model restrained the container count based on a user-inputted wing load. It assumed, from prior competitions, an aircraft empty weight of 7 *lb.* and applied equilibrium analyses to project the optimal flight conditions and raw scores for any feasible set-up.

The team then performed a statistical analysis of the 2017, 2018, and 2019 fly-off results to predict their placement within a normal scoring distribution. They confidently expect that their aircraft-- equipped with an efficient set-up-- can perform two standard deviations above the mission average. The team provided the model with thousands of sensor length ([11.0, 27.0] *in.*) and wing load ([2.5, 4.0] *lb./ft.²*) combinations and, for the second- and third-missions, chose the most efficient and reasonable of these as data. The indicated "design point" is the optimal configuration for which the aircraft's maximum gross weight is no heavier than 15.0 *lb.*

Figure 3.2.a illustrates the results of the scoring study in-full. **Table 3.2.1** details the parameters, flight conditions, and projected scores for the three previously-mentioned configurations.



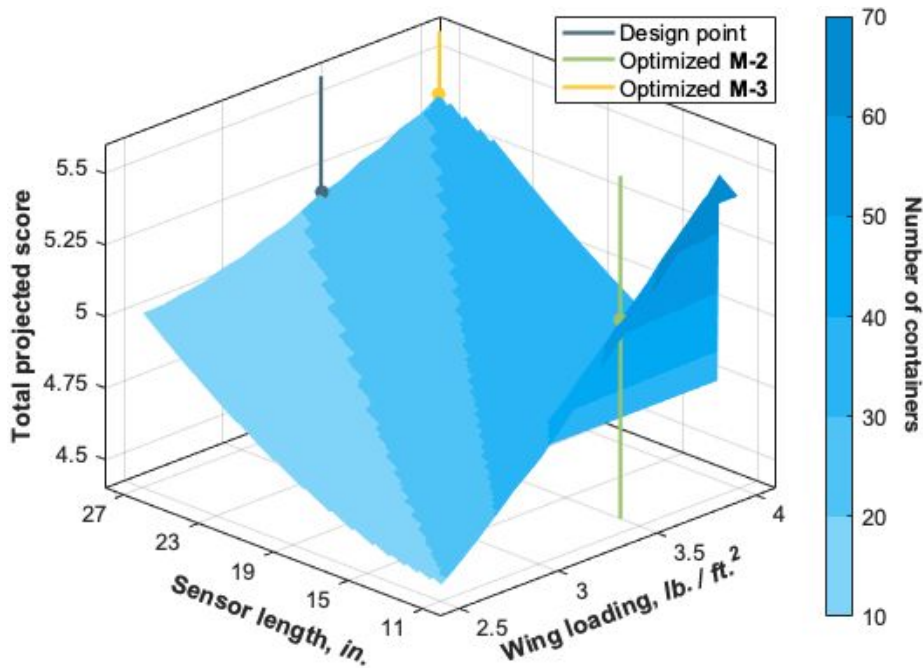


Figure 3.2.a: Total projected score sensitivity, with varying sensor length and wing loading.
The color gradient denotes the maximum container count for any configuration.

	Parameter	Design point	Optimal M-2	Optimal M-3
L_{SEN}	Sensor length	27.0 in.	12.0 in.	27.0 in.
v_{AV}	Average speed	101.2 ft./s.	102.7 ft./s.	109.5 ft./s.
	M-2	78.4 ft./s.	77.6 ft./s.	78.4 ft./s.
W_{G}	Gross weight	14.9 lb.	15.4 lb.	17.5 lb.
	M-3	9.0 lb.	8.8 lb.	9.0 lb.
nC	Number of containers	22	53	31
nL	Number of laps	18	18	18
Sc_{TOT}	Total projected score	5.2 of 7	5.1 of 7	5.4 of 7

Table 3.2.1: Parameters, flight conditions, and projected initial scores for the most efficient set-ups.

According to the study, smaller sensor sizes allow high container counts at the aircraft's most efficient loading configurations and produce optimal second-mission scores. Large sensors, due to their length and weight, give the best ground- and third-mission numbers. The team elected to design for the latter; in addition to the high final-flight score, the relatively low container count needed to attain the projected score makes the ground-mission easily optimizable.



3.3 · Translation into design requirements :: The design point detailed in **Table 3.2.1** poses the challenge of ensuring that an aircraft can safely carry 22, 27 *in.*-long sensor containers and attain the target score. The design of the fuselage and wing will have the highest influence on the aircraft's performance.

Fuselage :: The fuselage requires about 24 *in.*² of cross-sectional area and a minimum length of 28 *in.* to accommodate the containers of the 22 sensors for Mission 2. Additionally, the fuselage must have the strength to carry a distributed payload of 7 *lb*. The decision to include batteries, a towing mechanism, and other hardware components would add to the weight requirement of the fuselage to nearly 13 *lb*. The fuselage must also be structurally sound during maneuvers with a load factor no greater than 4.

Wing :: The design of the fuselage impacts the initial sizing of the wing. With any wing placement position, the airflow along the area of the wing that the fuselage would project on to will be severely affected by the presence of such a large fuselage; so much so that the wing can be regarded as not generating any lift at that area. Assuming a square fuselage, the effective wingspan would be 12 *in.* shorter. With the use of the entire allowable wingspan of 12 *in.*, the wingspan for wing sizing must be about 52.5 *in.*

3.4 · Configuration selection :: With the conclusion that the aircraft must have adequate cargo lifting capacity, UCSD DBF considered ten possible design elements that may impact a plane's payload capability: aircraft type, wing placement, wing shape, wingtips, empennage, propulsion system, fuselage shape, landing gear, sensor deployment opening, and deployment mechanism. To help them select an optimal design solution from a large field of configurations, the team has adopted and weighed several figures of merit, listed in **Figure 3.4.1**.

Figures of merit :: The team has concluded that it should give more consideration to capabilities and characteristics that have a greater impact on overall aircraft performance. The team assigned each of the five figures of merit a weight from 1× (least important) to 5× (most important). The selection and significance of each figure is based on the design requirements addressed in § 3.3. The weights assigned to each figure of merit establish a hierarchy of importance, determined by considering their impact on performance optimization in comparison to the team's time and resource constraints discussed and addressed in § 2.2.



Figure of merit	Weight	Biplane
Manufacturability	5×	Element is easy to manufacture; process is not time-consuming.
Repairability	4×	Lift is optimized on lifting surfaces; drag is minimized.
Structural loading	3×	Element is easy to repair, should it be damaged in any capacity.
Flight stability	2×	Loads are transferred to structural elements, preventing breakage.
Total score	1×	Aircraft retains greater control during maneuvers and steady flight.

Table 3.4.1 · The five figures of merit in consideration, with given weight and description.

Selection process :: For each figure of merit, each configuration is rated from 1 (low design favorability) to 5 (high design favorability). Their scores are defined as the sum of the products of the figure of merit's weights and ratings. The team has selected the configuration with the highest score. The order of evaluation for each configuration is deduced by from the highest to lowest number of dependencies a configuration has to the rest.

Aircraft type :: The main considerations for aircraft configurations were manufacturability and repairability. The team chose a monoplane because the configuration provides greater payload capacity for longer sensors while still staying within the 5 ft. maximum wingspan criteria. Both a flying wing and a lifting body would need to be scaled up significantly to accommodate the same size sensor as a monoplane layout. Additionally, both the flying wing and lifting body configuration do not satisfy the two main considerations due to their complexity in form and precision required for subsystem interface.



Figure of merit	Monoplane	Biplane	Flying wing	Lifting body
Manufacturability	5×	5	4	2
Aerodynamics	4×	4	3	5
Repairability	3×	5	4	1
Structural loading	2×	2	5	2
Flight stability	1×	4	4	1
Total score		64	58	38
				41

Table 3.4.2 · Figure of merit matrix for the aircraft configuration.



Wing placement :: When selecting wing placement, the team was most concerned with aerodynamic performance when paired with a large fuselage. This heavily impacts the amount of lift the wing is capable of producing. A high or parasol wing has the added advantage of having better roll stability in gusts by having the center of mass be located below the center of pressure via the keel effect. In addition, having a mid wing would limit the amount of usable space within the fuselage. Between a high and parasol wing, a high wing was determined to be easier to manufacture and mount.

Figure of merit		Low-wing	Mid-wing	High-wing	Parasol wing
Manufacturability	5x	4	1	5	2
Aerodynamics	4x	2	3	4	5
Repairability	3x	4	2	4	5
Structural loading	2x	4	5	4	3
Flight stability	1x	3	2	5	4
Total score		51	35	66	55

Table 3.4.3 · Figure of merit matrix for the wing placement.

Wing shape :: The shape of the wing was decided by the stall performances of each wing. While an elliptical wing has the most aerodynamic efficiency at cruising speed, it has poor stall characteristics when compared to a rectangular and trailing tapered wing. The straight leading edge of both configurations have the stall starting at the root of the wing and moving outwards instead of at the tip. A tapered trailing edge wing will have the stall forming at the root of the wing while still retaining the low drag characteristics of a traditionally tapered wing. Additionally, a tapered wing requires a larger surface area to produce the same amount of lift compared to a rectangular wing, which significantly increases the weight of the wing.

Figure of merit		Rectangular	Tapered	Elliptical	Swept
Manufacturability	5x	5	4	1	3
Aerodynamics	4x	4	4	5	4
Repairability	3x	4	4	2	2
Structural loading	2x	4	4	3	1
Flight stability	1x	3	5	4	2
Total score		64	61	41	41

Table 3.4.4 · Figure of merit matrix for the wing shape.



Empennage :: The largest design consideration for the empennage configuration was flight stability to address the turbulent airflow caused by the fuselage and dual tractor propulsion setup. A T-tail setup raises the horizontal stabilizer above the turbulent air but has a super stall characteristic at high angles of attack. Although a cruciform tail is not as susceptible to super stalls, this configuration was considered difficult to manufacture and even harder to repair. In turn, the team chose a T-tail design.



Figure of merit	Conventional	Cruciform	T-tail	V-tail
Manufacturability 5x	5	2	4	2
Aerodynamics 4x	2	4	4	3
Repairability 3x	4	2	3	3
Structural loading 2x	4	4	3	2
Flight stability 1x	2	4	5	3
Total score	55	44	56	38

Table 3.4.5 · Figure of merit matrix for the empennage.

Propulsion system :: The propulsion systems were scored based on aerodynamic efficiency and thrust output, which a dual tractor setup was deemed best suited for while maximizing the thrust capacity of the plane. In order for a tractor setup to achieve enough static thrust the team wanted, a large propeller and landing gear setup was needed which increases the drag and reduces the aerodynamic efficiency of the plane. A dual tractor setup has the electronic advantage of splitting up the load between two ESCs and motors, reducing the total temperature of the electronics.

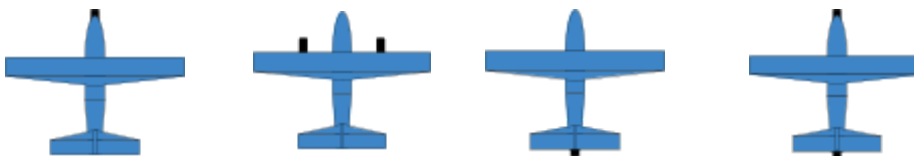


Figure of merit	Tractor	Dual tractor	Pusher	Tractor-pusher
Manufacturability 5x	3	4	2	1
Aerodynamics 4x	3	4	5	3
Repairability 3x	4	3	3	2
Structural loading 2x	5	2	3	4
Flight stability 1x	4	5	3	2
Total score	53	54	48	22

Table 3.4.7 · Figure of merit matrix for the propulsion system.



Wingtips :: The team weighed a wingtip's manufacturability most heavily when considering different wingtip configurations. Rounded and hoerner wingtips are time consuming and difficult to fabricate. Also, winglets are most difficult to repair in the case of a crash. Therefore blunt wingtips were chosen.



Figure of merit	Blunt	Rounded	Hoerner	Winglet
Manufacturability 5x	5	4	1	2
Aerodynamics 4x	2	4	5	5
Repairability 3x	5	4	3	2
Structural loading 2x	4	3	3	5
Flight stability 1x	2	3	3	4
Total score	58	57	43	50

Table 3.4.6 • Figure of merit matrix for the wingtips.

Fuselage form :: Cargo capacity and drag characteristics were the main factors in deciding the general shape of a fuselage. The presence of landing gear also led to the consideration of how the two elements would be placed and secured with respect to one another. In order to minimize the cross sectional area of the fuselage, a square fuselage seemed to be most favorable. However, a square fuselage with rounded edges was selected for its superior drag characteristics, as well as having stress concentrations at the corners. An elliptical or circular fuselage would need a greater cross sectional area to store the same number of sensors for Mission 2.



Figure of merit	Square	Square-ellipse	Ellipse	Circular
Manufacturability 5x	4	3	1	2
Aerodynamics 4x	2	3	4	4
Repairability 3x	4	4	3	2
Structural loading 2x	4	3	3	4
Flight stability 1x	2	3	3	4
Total score	46	48	39	44

Table 3.4.8 • Figure of merit matrix for the fuselage form.



Landing gear :: The landing gear of the aircraft were selected due structural loading and flight stability considerations. A tricycle gear has the most stability both during take off and landing. A tricycle gear would prevent ground looping, an effect where aerodynamic forces cause the advancing wing to rise and the other wingtip to strike the ground seen with a tail dragger configuration. The high wing configuration of the aircraft requires long supports for the landing gear at the wingtips for the tip tricycle and tip tail dragger configuration, which results in significantly high and unfavorable amounts of form drag.



Figure of merit	Tricycle	Tip-tricycle	Tail dragger	Tip-tail dragger
Manufacturability 5x	4	1	3	1
Aerodynamics 4x	3	1	4	2
Repairability 3x	4	2	4	2
Structural loading 2x	4	2	3	2
Flight stability 1x	4	2	3	2
Total score	56	21	52	25

Table 3.4.9 · Figure of merit matrix for the landing gear.

Sensor deployment opening :: Manufacturability and repairability were the main factors in deciding the configuration of the opening that allows for sensor deployment during Mission 3. Bomb bay doors and a rear cargo door require allocation of space and weight for the hardware that would allow them to function, decreasing the number of containers the aircraft can carry, an issue shared by a ducted bottom opening. Also, the complexity of the mechanisms heavily affect the configurations' manufacturability and repairability. Thus, an open bottom was selected for its simplicity with acceptable effects on aircraft drag.



Figure of merit	Bomb bay doors	Open bottom	Ducted bottom	Read cargo door
Manufacturability 5x	1	5	4	2
Aerodynamics 4x	5	1	3	4
Repairability 3x	1	5	3	2
Structural loading 2x	5	3	2	4
Flight stability 1x	4	2	4	4
Total score	42	52	49	48

Table 3.4.10 · Figure of merit matrix for the sensor deployment opening.



Deployment mechanism :: The largest design consideration for the deployment mechanism was the flight stability of the sensor while being towed during Mission 3. A dual reel or dual spool configuration provides superior flight stability of a deployed sensor compared to having only one tether. However, reels exhibit unfavorable stowing characteristics when retracting the sensor where the tether may wrap on top of itself if not precisely guided. The elongated form of a spool allows for easier tether guidance during deployment, towing, and retraction of the sensor, thus the choice for a deployment mechanism.



Figure of merit	Reel	Dual reel	Spool	Dual spool
Manufacturability 5x	4	3	3	2
Aerodynamics 4x	4	3	4	3
Repairability 3x	2	3	2	4
Structural loading 2x	2	3	4	5
Flight stability 1x	1	5	1	5
Total score	47	46	46	49

Table 3.4.11 · Figure of merit matrix for the deployment mechanism.

3.5 · Final conceptual design :: In accordance with the scoring methodology analysis (§ 3.1-3.3), and after considering many design configurations (§ 3.4), the team will pursue an aircraft design with a monoplane aircraft configuration, high-wing placement, T-tail, rectangular wing planform, dual-tractor motors, square fuselage with rounded edges, tricycle landing gear, an open bottom fuselage, and a dual spool tether towing mechanism.



Figure 3.5.a · CAD render of selected configurations.



§ 4 Preliminary design

4.1 - Overall design methodology :: Based on prior experience, UCSD DBF developed an iterative design process. The scoring analysis drove them to consider and select the most optimal configurations for the aircraft, as described in § 3. In the preliminary design phase, the team used the contest constraints to size the aircraft's fuselage and lifting surfaces; they also conducted a propulsion system analysis to select the most efficient arrangement. The team scrutinized this configuration to ensure that it satisfied design requirements and simulated its performance in a team-developed flight model.

In the detail design phase, the team finalized the process and designed the aircraft's component and subsystem architecture. After fabricating and assembling the plane, the team validates their design and tests each component before the first test flight.

4.2 - Design and trade studies :: The team selected an optimal arrangement for the aircraft's propulsion system and used the fly-off constraints to size its fuselage and wing.

Propulsion system :: To select a battery, motor, and propeller, the team implemented an optimization algorithm. Because it seemed naïve to choose the first arrangement that met their requirements, the team developed a new design methodology. Thus, they followed a multi-disciplinary design optimization (MDO) problem described by Hwang et al. at the University of California, San Diego [1]:

maximize	net efficiency, defined in Equation 4.1
with respect to	propeller and motor choice
subject to	cruising conditions

$$\eta_{NET} = \eta_{PROP} * \eta_{MOTOR} = \frac{U_e T}{V I} \quad \text{Equation 4.1}$$

Assuming that the aircraft cruises at a steady-state condition when airspeed and thrust are constant, and neglecting the decay in voltage through the flight, the net efficiency is optimized with a minimized current draw. Such a configuration would also boost the aircraft's endurance and greatly benefit the team's third-mission performance.

With this in mind, the team inputted battery performance data from various hobby store websites, motor performance equations and data from Bunge at Stanford University [2] and Scorpion documentation [3], and propeller performance data from APC [4] into their algorithm. In all, the team analyzed nearly 20,000 different propulsion system combinations. **Figure 4.1.a** charts a visualization of the simulation results that were completed for each mission. **Table 4.1.1** shows the results of this optimization.



Component or parameter	Optimal M-1	Optimal M-2	Optimal M-3
Battery Specifications		Glacier 30C 6s 4500 mAh, 22.2 V, lithium-polymer	
Motor Specifications		Scorpion SII-4020 420 Kv	
Propeller, from APC	11 in. × 6 in.	12 in. × 10 in. -E	11 in. × 7 in. -E
W _{PROP}	37.8 oz.	37.3 oz.	37.2 oz.
η _{NET}	0.647	0.714	0.643

Table 4.1.1 · Most efficient propulsion system configurations for each mission.

Fuselage sizing :: While they wanted to build a fuselage large enough to accommodate 22 sensors according to the conceptual design point (proposed in § 3.2), the team decided that such a large shape would cause a significant amount of drag and detrimentally impact the aircraft's performance and score. Thus, they settled on a fuselage with a 30 in. long, 6 in. tall, and 6 in. wide internal compartment, large enough to fit 10 sensors.

The team can achieve a highly competitive fly-off score with refinements to the sensor's material design.

Wing sizing :: The team expected the fuselage's necessary irregular, large shape to produce a large amount of drag, prompting their decision to design a rectangular wing to maximize the aircraft's lift. But since this solution also causes more induced drag, they opted for a wing with a larger aspect ratio. The team needed to strike a balance between the wing's area and span.

From this maximum allowable wingspan of 60 in., historically-observed target airspeed (95 ft./s.) and target lift coefficient (0.28), the team determined that their ideal aspect ratio is 5 and chord length is 12 in. The team also calculated expected cruise conditions, including a reduced Mach number (0.045) and a reduced Reynolds number (367,000). They use these findings extensively in their aerodynamic analyses.

4.3 · Aerodynamic analyses :: To obtain the non-dimensional coefficients of interest for lift, drag, and moment, the team used computational fluid dynamics (CFD) analysis in the XFLR5 software program; such a study produced a wide range of lift and drag distributions relative to various cruise speeds. Where XFLR5 fell short, the team resorted to a component-wise drag build-up analysis to more accurately predict the aircraft's aerodynamic performance.

Airfoil selection :: UCSD DBF evaluated thousands of airfoils through the XFOIL program, aiming to create a shortlist of the most lift-efficient ones. After executing the analysis at expected cruise conditions, the team ranked the airfoils by the highest glide ratio (L / D). The aircraft's structural integrity and the team's manufacturing capacity further restricted the selection to airfoils with a thickness greater than 9 %.



These constraints sufficiently narrowed the scope down to several airfoils that the team further analyzed. To gauge the performance of those selected, the team conducted fixed-weight, infinite- and finite-wing analyses on the airfoils in XFLR5. **Figure 4.3.a** compares the geometries according to these findings.

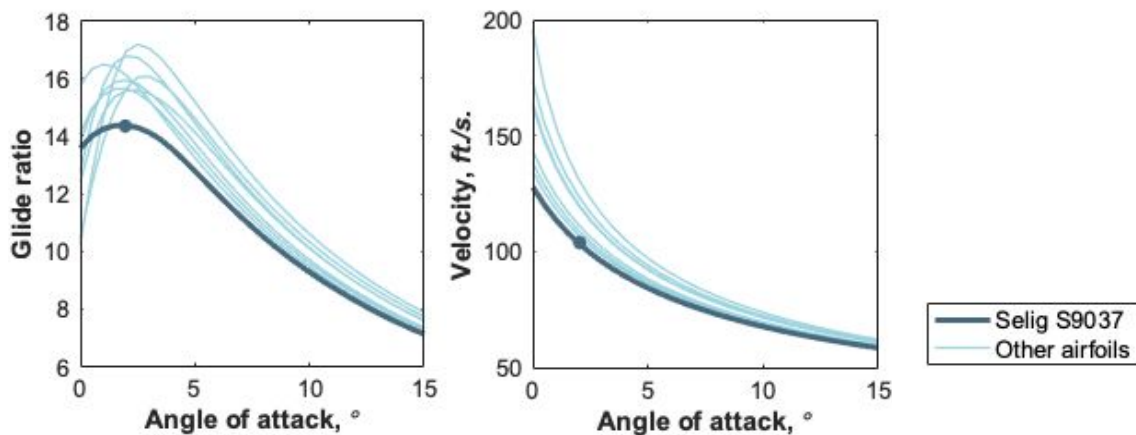


Figure 4.3.a: XFLR5-generated finite-wing analysis of shortlisted airfoils. The conditions at the cruising angle of attack of 2° are also marked.

While these analyses predicted these airfoils would exhibit similar lift performances, they also suggested the aircraft would need to maintain quite different speeds ([102, 132] ft./s.) at the cruising angle of attack of 2° depending upon the airfoil. Because their pilot felt uncomfortable handling a plane at speeds that far exceeded an ideal 95 ft./s., the team elected to use the S9037 airfoil, whose geometry best addressed these concerns according to the XFLR5 analysis.

Lift :: After selecting the S9037 airfoil, the team used XFLR5 to simulate their aircraft's lift performance. As the program poorly estimates the characteristics of other components that make relatively negligible impacts, the team applied the lifting surface analysis only to the wings. They also modeled a gap in the input, shown in **Figure 4.3.b**, to account for the fuselage's influence on the flow. **Figure 4.3.c** details the aerodynamic coefficient plots for each mission configuration, as obtained from this analysis.

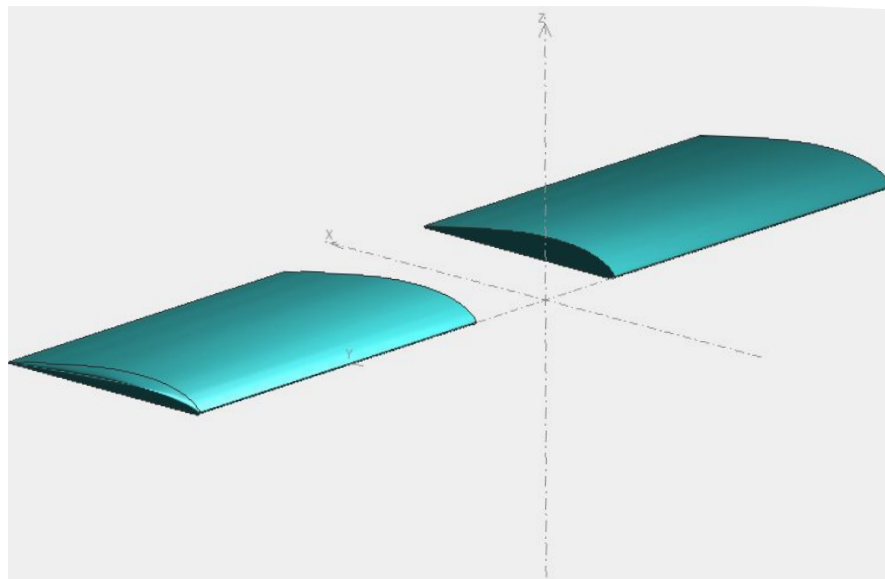


Figure 4.3.b · Lifting surface analysis, as inputted into XFLR5.

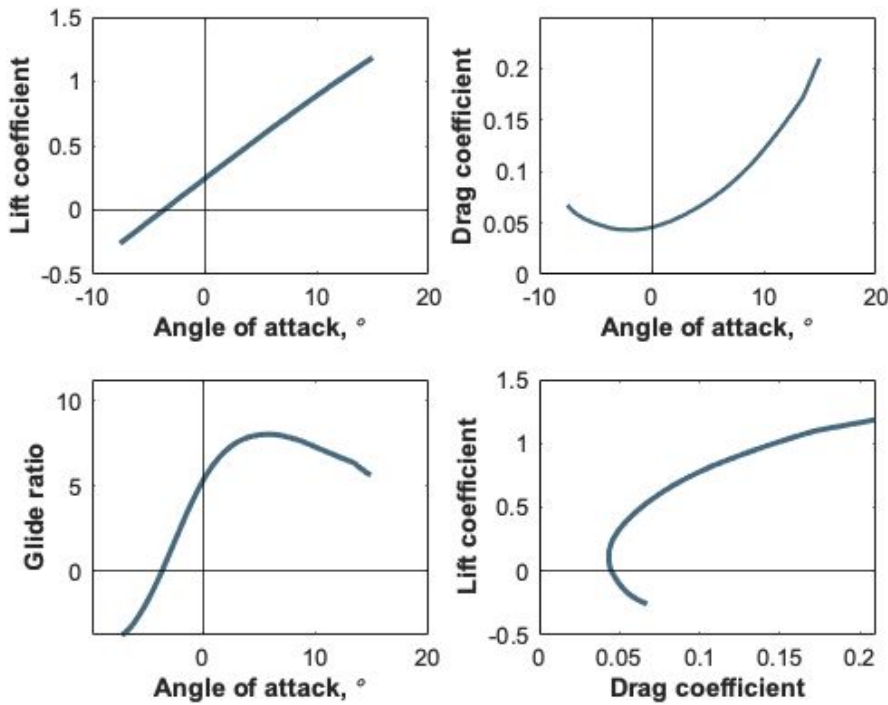


Figure 4.3.c · XFLR5-generated aerodynamic coefficient plots for a fixed weight of 14.9 lb.

Using the basic lift equation, the team derived a relationship between the aircraft's speed at certain angles of attack and its weight. **Table 4.3.1** more finely summarizes the aircraft's aerodynamic characteristics for the conditions that the team expects to encounter.

Condition		Angle of attack	Lift coefficient	Velocity
$*_{CR}$	Cruise conditions	M-1	2 °	0.277 69.4 ft./s.
		M-2	2 °	0.277 101.6 ft./s.
		M-3	2 °	0.277 78.8 ft./s.
$*_{ST}$	Stall conditions	M-1	14 °	1.185 40.3 ft./s.
		M-2	14 °	1.185 59.0 ft./s.
		M-3	14 °	1.185 45.7 ft./s.
$*_{TO}$	Takeoff conditions	M-1	2 + 35 °	1.255 32.6 ft./s.
	Flaps down at 35 °	M-2	2 + 35 °	1.255 47.7 ft./s.
		M-3	2 + 35 °	1.255 37.0 ft./s.

Table 4.3.1 Angle of attack, lift coefficient, and velocity at various flight conditions.

Drag :: As XFLR5 infamously underestimates its component drag computations, the team calculated the drag build-up by hand, according to equations that Sholz at the Hamburg University of Applied Sciences curated [5]. By neglecting smaller contributions, parasitic and induced components comprise the drag that the aircraft experiences.

As shown in **Equation 4.2**, a component's parasitic drag is the product of its skin-friction drag, pressure drag, wetted-to-reference area ratio, and flow interference from adjacent structures. During the third-mission, the sensor-- modeled here as a cylindrical object-- also experiences this kind of air resistance. Assuming that the flow surrounding the aircraft is turbulent, the contribution of the flow-induced shear force, inversely relates to the logarithm of the associated Reynolds number (described in **Equation 4.3**).

$$C_{D,0} == \sum_{c=1}^n C_{f,c} FF_c \frac{S_{wet,c}}{S_{ref}} Q_c + C_{D,SEN} \quad \text{Equation 4.2}$$

$$C_{f,turbulent} == \frac{0.455}{[\log(Re)]^{2.58}} \quad \text{Equation 4.3}$$

The form factor represents the build-up in pressure along the surface of a component, which also causes drag. The wing and empennage form factor is dependent on the flow's Mach number, the location of the airfoil's thickest point, and its maximum thickness-to-chord length ratio (**Equation 4.4**). For the fuselage, this factor depends only upon the fineness ratio (**Equation 4.5**). The Sholz document provided estimates of the flow's interference factor.

Finally, in his 1965 textbook *Fluid-Dynamic Drag*, Hoerner [6] estimates that the drag coefficients of long, blunt cylindrical bodies, like the sensor, converge to a near-constant value of 0.81 for fineness ratios greater than 5. Thus, the team calculated the drag that the deployed sensor experiences. As its actual geometry includes a nose cone and other features that reduce pressure drag, they expect this value to be an overestimate.

All of these non-dimensional values are tabulated in **Table 4.3.2**.

$$FF_{E/W} == [1 + \frac{0.6}{x_t} \frac{l}{c} + 100 (\frac{l}{c})^4] \cdot [1.34 M^{0.18}] \quad \text{Equation 4.4}$$

$$FF_F == 1 + \frac{60}{(l_f/d_f)^3} + \frac{(l_f/d_f)}{400} \quad \text{Equation 4.5}$$

Parameter		Fuselage	Wing	Horizontal stabilizer	Vertical stabilizer	Total
$C_{D,0}$	Zero-lift drag coefficient	M-1 M-2 M-3	0.01162 0.00804 0.01136	0.01502 0.01393 0.01465	0.00369 0.00341 0.00360	0.00199 0.00184 0.00194
						0.03232 0.02723 0.03155
						--
C_f	Turbulent skin-friction drag coefficient	M-1 M-2 M-3	0.00383 0.00358 0.00375	0.00523 0.00485 0.00510	0.00575 0.00532 0.00561	0.00564 0.00522 0.00550
						--
						--
$FF_{F/E/W}$	Form factor		1.159	1.196	1.101	1.101
θ	Interference factor		1.00	1.20	1.03	1.03
						--

Table 4.3.2. Non-dimensional drag parameters for each of the aircraft's components.

Meanwhile, the magnitude of induced drag-- or the resultant drag created by the presence of lift-- is known to be quadratically proportional to the lift coefficient; it also inversely relates to the aircraft wing's aspect ratio and the Oswald efficiency factor (**Equation 4.6**). The Sholz document suggested that this factor depends upon the total number of engines and the wing's aspect, taper, and thickness-to-chord length ratios (**Equation 4.7**). The induced and total drag coefficient values for each configuration are documented in **Table 4.3.3**.

$$C_{D,i} == \frac{C_L^2}{\pi e AR} \quad \text{Equation 4.6}$$

$$e == \frac{1}{(1 + 0.12 M^6) \left[1 + 0.142 + f(\lambda) AR \left(\frac{l_0 t}{c} \right)^{0.33} + \frac{0.1(3N_e + 1)}{(4 + AR)^{0.8}} \right]} \quad \text{Equation 4.7}$$



Parameter	M-1	M-2	M-3
e Oswald efficiency factor	0.83879	0.83879	0.83879
$C_{D,0}$ Zero-lift drag coefficient	0.03232	0.02723	0.03155
$C_{D,i}$ Induced drag coefficient	0.00667	0.00667	0.00667
C_D Total drag coefficient	0.03900	0.03390	0.03822

Table 4.3.3 · Efficiency factor and drag coefficients for each mission configuration.

4.4 · Stability and control analyses :: To ensure that their aircraft can fly steadily without unaccounted erratic movements and satisfy longitudinal stability, the team analyzed the pitching moment and static margin of their aircraft. The XFLR5 analysis found the aircraft's neutral point to be 10.5 in. from its leading edge. After defining the desired center of gravity for each mission, the team calculated the expected static margin. **Table 4.4.1** documents these outcomes; that each margin is positive implies that the aircraft's center of gravity is in front of its neutral point.

Parameter	M-1	M-2	M-3
x_{CG} Center of gravity	3.0 in.	4.0 in.	3.5 in.
SM Static margin	62.3 %	53.9 %	58.1 %

Table 4.4.1 · Stability and control parameters for each mission configuration.

The aircraft is statically stable when its pitch-moment curve slope is negative when its zero-lift pitch-moment coefficient is zero. The program-generated moment coefficient plots, shown in **Figure 4.4.a**, suggested that this condition is satisfied for each configuration.

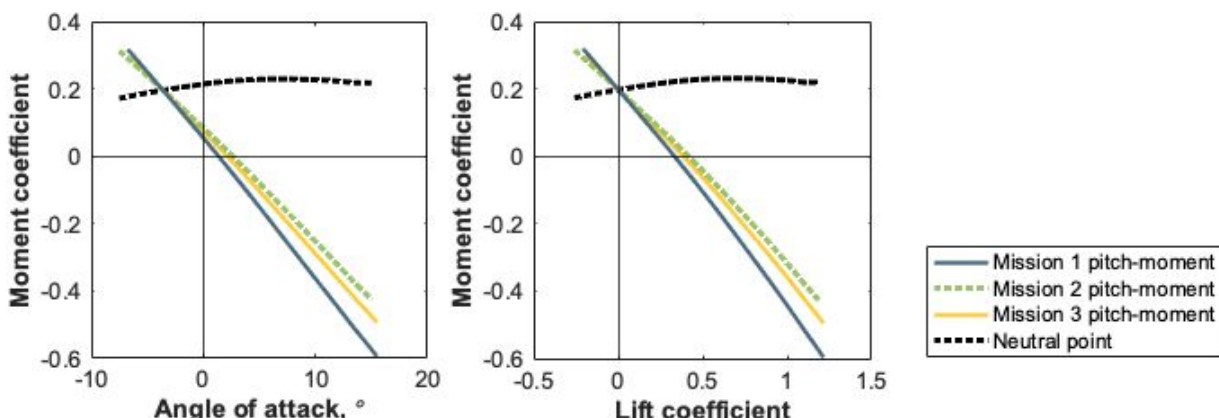


Figure 4.4.a · XFLR5-generated moment coefficient plots.



Lastly, the overall pitch-moment acting on a stable aircraft should be zero. **Figure 4.4.a** suggests that its zero-moment angles of attack range between [1.4, 2.6]°; it increases with each subsequent mission configuration. To compensate, the team must manually trim the tail, using an incidence angle or an elevator flap to shift the moment coefficient to zero at an angle of attack of 0°.

4.5 - Mission model :: The team developed a mission model in MATLAB using slightly more advanced equilibrium analyses than they did in their scoring study (§ 3.3). The model determined the speeds at which the aircraft must fly during the 1000 ft.-long straights (**Equation 4.8**) and the banked-angle turns (**Equation 4.9**), based on user-inputted mass and maximum load factor values. Using these produced velocity estimates and the flight path as defined in **Figure 3.1.a**, it calculated the total mission time and other relevant quantities. They then applied the scoring study's statistical analysis to refine its total fly-off score projection.

$$V_{STRAIGHT} == \sqrt{\frac{2 m g}{\rho_{air} S C_L}}$$
 Equation 4.8

$$V_{TURN} == \sqrt{\frac{2 m g}{\rho_{air} S C_L \cos(\theta)}}$$
 Equation 4.9

In this model, the largest sources of uncertainty arise from challenges to this simple equilibrium analysis, like manufacturing tolerance, pilot input, and unaccounted forces. Location- and time-based differences between test sessions in San Diego and San Ramon and the planned fly-off in Tucson-- such as field altitude (ranging between [62, 2,389] ft.) and air temperature (averaging between [60, 82] °F)-- may also propagate uncertainty. The team couldn't test a preliminary prototype due to the fabrication limitations caused by the COVID-19 pandemic; thus, they more warily considered these uncertainties when relying upon the model.

Tables 5.5.1 and **5.5.2**, in later sections, present a complete overview of this model's outputs.



§ 5

Detail design

In the detail phase of their design process, UCSD DBF finalized design decisions. They analyzed the structural capabilities and flight performance of their aircraft and determined the architecture of the sensor, its deployment mechanism, and other subsystems.

5.1 - Final design parameters :: Tables 5.1.1 and 5.1.2 summarize the aircraft's dimensions, design characteristics, and electrical specifications.

Dimension	Fuselage	Wing	Horizontal stabilizer	Vertical stabilizer	Total
b or L	Span or length	61.5 in.	60.0 in.	24.0 in.	12.0 in. 58.0 in.
H	Height	8.0 in.	--	--	-- 24.0 in.
W	Width	6.0 in.	--	--	-- 60.0 in.
C_{root}	Root chord	--	12.0 in.	8.5 in.	9.0 in. --
C_{tip}	Tip chord	--	12.0 in.	6.5 in.	7.5 in. --
MAC	Mean aerodynamic chord	--	12.0 in.	7.5 in.	8.3 in. --
S	Reference area	--	4.4 ft. ²	1.3 ft. ²	0.7 ft. ² --
b^2/S	Aspect ratio	--	5.7	3.2	2.9 --
	Airfoil				Selig S9037

Table 5.1.1 · The aircraft's final dimensional characteristics. Values listed as applicable.

Tail servomotors	KST X08H	ESC	Frsky Neuron
Stall torque	73.6 oz.-in. at 8.4 V	Current rating	80.0 A
Servomotor speed	0.09 sec/60° at 8.4 V	Battery	Glacier 6s
Servomotor weight	0.335 oz.	Number of cells	6 series × 2 parallel
Wing servomotors	KST X10 Mini	Pack voltage	22.2 V
Stall torque	104.2 oz.-in. at 8.4 V	Pack weight	46.0 oz.
Servomotor speed	0.09 sec/60° at 8.4 V	Motor	Scorpion SII-4025
Servomotor weight	0.811 oz.	Kv rating	420

Table 5.1.2 · Electrical and mechanical specifications of the aircraft.

5.2 - Structural characteristics and capabilities :: UCSD DBF examined how the aircraft's structural loads-- resulting from ground impact upon landing, aerodynamic and motor thrust stresses-- are applied and distributed throughout the airframe. **Figure 5.2.a** presents a diagram of these forces. To account for the large forces expected during flight, the team implemented a few critical design aspects to ensure that the system does not fail; subsequent sections describe these solutions in extensive detail.

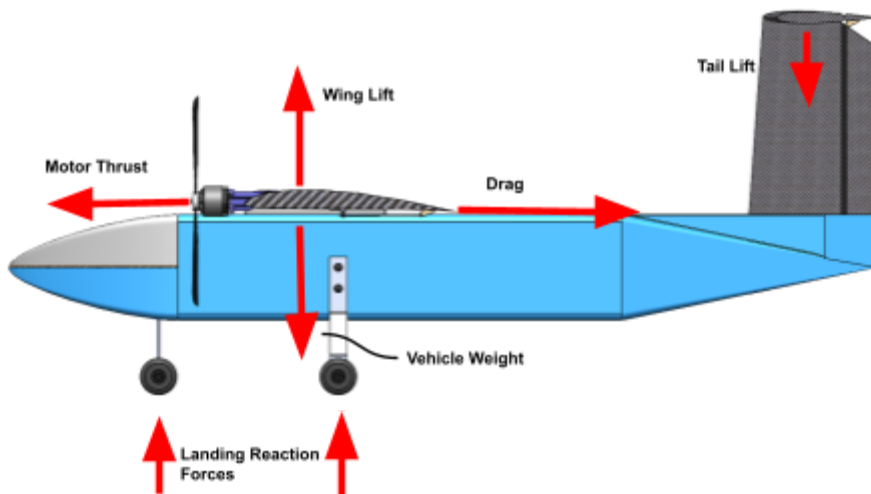


Figure 5.2.a · Free-body diagram of the aircraft.

In evaluating the aircraft's aerodynamic and structural operating limits, the team conducted an operating envelope analysis. Based on historical data, the team determined that the aircraft can maneuver at load factors up to 4 g; the never-exceed speeds for each mission are 120 % of that at cruise ([83.2, 122] ft./s.). As the first- and third-mission envelopes are quite similar, **Figure 5.2.b** illustrates their results as a combined analysis.

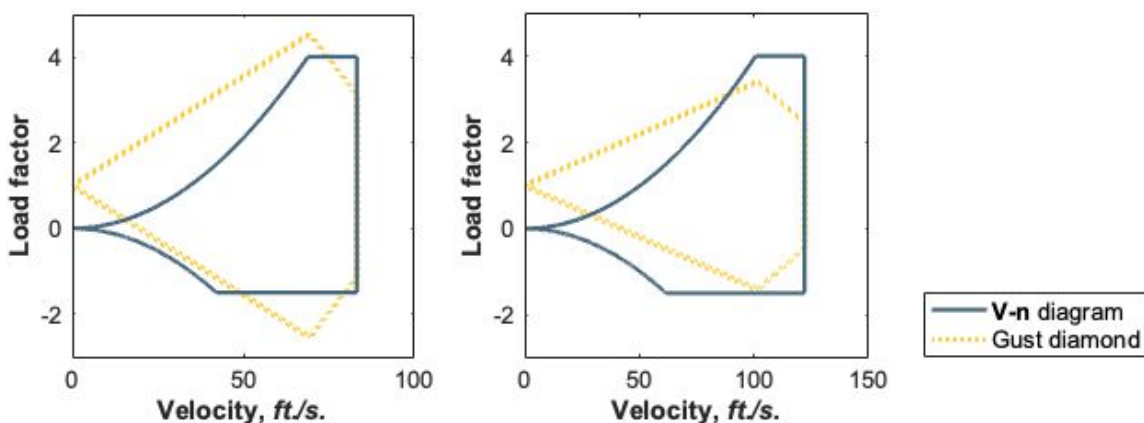


Figure 5.2.b · Velocity-load factor diagrams and gust diamonds for M-1, M-3 (left), and M-2 (right).



5.3 · System and subsystem architecture :: The team finalized their design process by thoroughly investigating the mechanics of its subsystems and the implementation of its avionic system.

Fuselage :: The team designed the aircraft's fuselage to maximize its payload carrying space. As presented in **Figure 5.3.a**, it consists of a foam board, fiberglass, monocoque structure; such a set-up offers an exceptional strength-to-weight ratio.

Its internal storage compartment, shown in **Figure 5.3.b**, is 30 in. long, 6 in. tall, and 6 in. wide-- large enough to fit the deployment mechanism and 10 shipping containers. A cutout on the bottom edge of the compartment, 3.5 in. wide and 30 in. long, allows the team to install, deploy, and retract payloads with minimal drag-producing turbulent airflow. Cross-sections of the fuselage's nose and tail are aerodynamic, further reducing drag effects; a cutout in its nose provides a mounting location for the aircraft's batteries and avionic equipment. Two bars, screwed into place at the bottom of the fuselage cutout, secure the payload; such a tight payload package prevents the center of gravity from shifting.

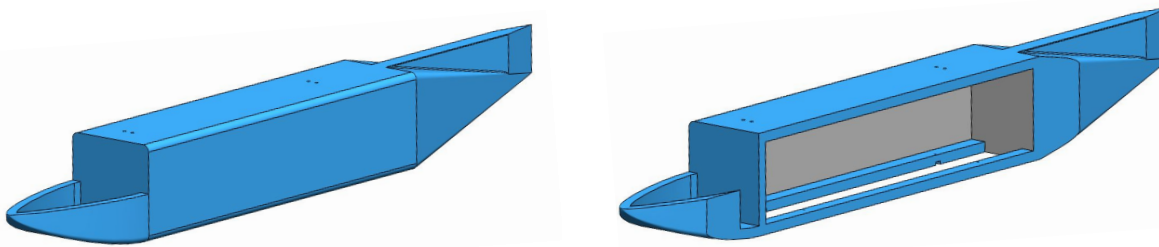


Figure 5.3.a · The aircraft's fuselage.

Figure 5.3.b · Cross-section of the aircraft's fuselage, revealing the interior compartment.

The aircraft's batteries, electronic speed controllers, and receiver mount to a $\frac{1}{8}$ in. thick basswood plate at the fuselage's nose. Velcro straps wrap around the batteries and through slots in the plate to secure them. Adhesive tape at the seams attaches the canopy of the battery compartment to the fuselage.

Figure 5.3.c presents an interior view of the compartment.

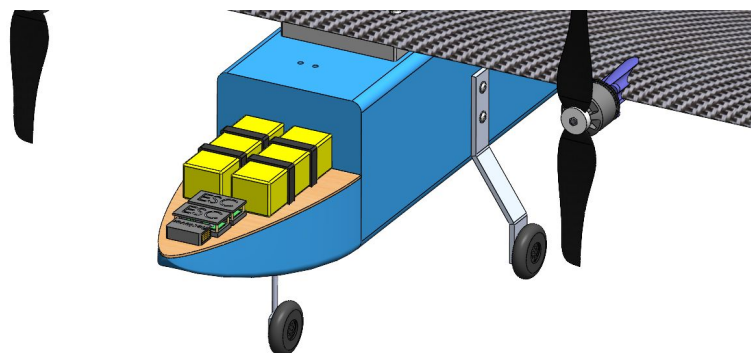


Figure 5.3.c · Internal view of the battery compartment.





Wing :: Four bolts fastened the aircraft's foam core, laminate wing to the top surface. These bolts pass through the wing and thread into nuts embedded into the fuselage foam providing a strong connection between fuselage and wing. A 3D-printed PLA filament adapter plate conforms to the airfoil, allowing the team to maintain their desired angle of incidence of 2° . **Figure 5.3.d** shows the wing configuration.

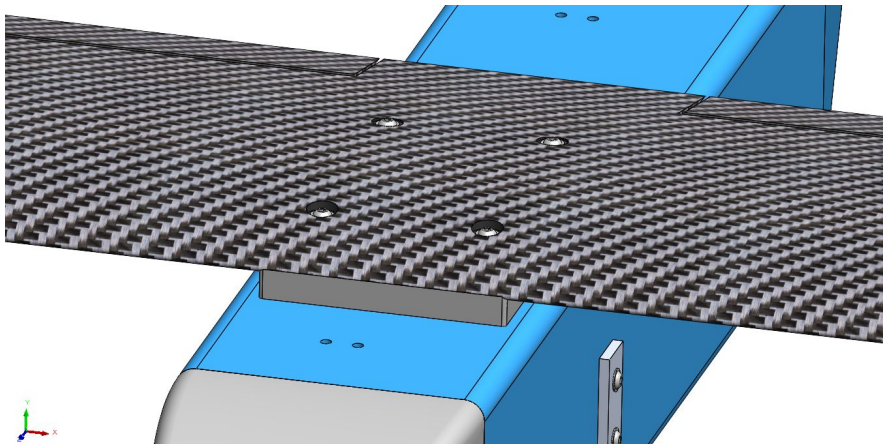


Figure 5.3.d · View of the wing and its mounting configuration.

Empennage :: The team determined that a T-tail style empennage was the most optimal configuration for our aircraft; this configuration allows the horizontal stabilizer to be well-above the turbulent air created from the fuselage and propellers. Threaded rods, embedded in the vertical stabilizer, pass through holes drilled in the fuselage's tail. A flat plate embedded in the fuselage tail provides a location for hex nuts to thread onto the rods, fastening the empennage onto the fuselage for a strong and reliable connection.

Figure 5.3.e and **5.3.f** demonstrate the empennage's arrangement.

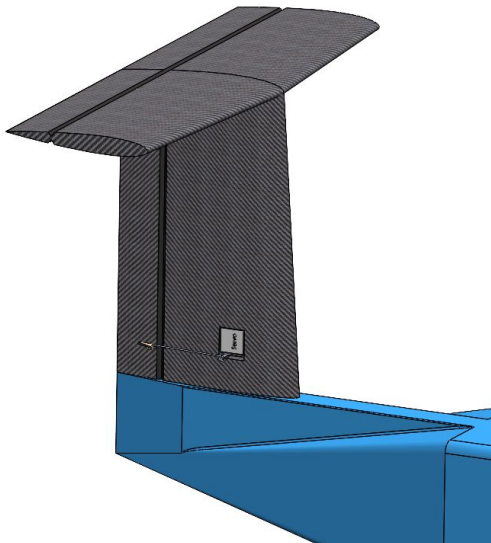


Figure 5.3.e · View of the empennage configuration.

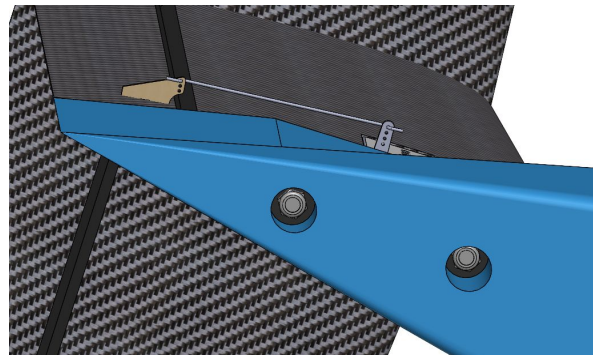
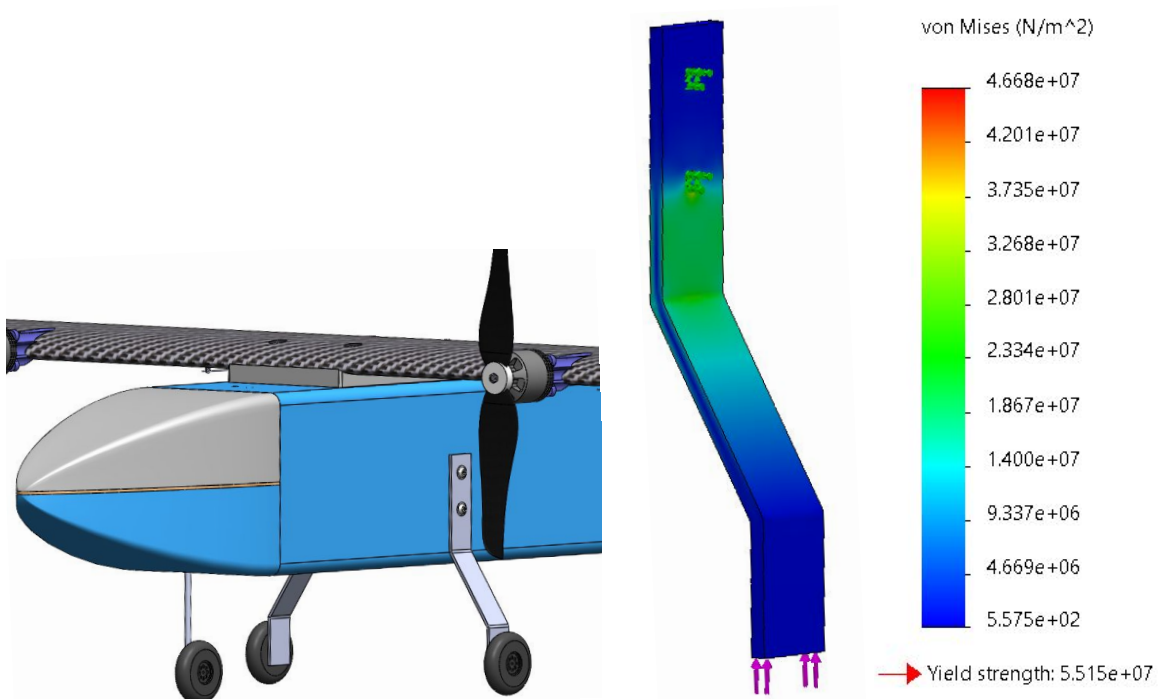


Figure 5.3.f · View of the empennage fasteners.



Landing gear :: The landing gear's tricycle configuration is simple, is lightweight, provides excellent ground tracking, and allows for ample clearance between the ground and propeller. A SolidWorks von Mises stress simulation, shown in **Figure 5.3.h**, suggested that the main wheels' aluminum struts can support loads up to 9 lb.-- twice the expected maximum.

The main wheels, placed slightly behind the aircraft's center of gravity, are fastened to the fuselage with two bolts, which thread into fasteners embedded into the fuselage's foam board. The nose wheel is embedded and adhered to the foam-fiberglass fuselage. **Figure 5.3.g** provides a closer view of the total landing gear configuration.



[**Figure 5.3.g**](#) · The aircraft's landing gear.

[**Figure 5.3.h**](#) · SolidWorks stress simulation of the landing gear.

Motor mount :: The team created a 3D-printed PLA motor mount that adapts to the wing airfoil's profile and screws onto the motor. To attach the motor mount, the team cut the wing's carbon fiber shell, exposed its foam core, adhered the motor mount onto the structure using an epoxy resin and carbon fiber fabric. This design, shown in **Figure 5.3.h**, ensured that the mount could withstand motor-induced tensile and torsional stresses.

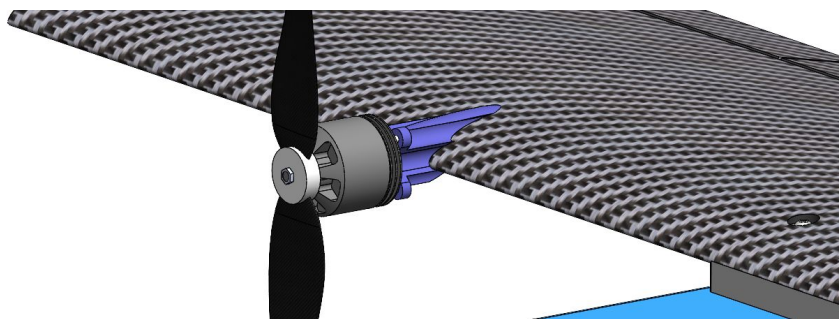


Figure 5.3.h: View of the motor mount.

Sensor :: The team opted to create the 27 in. sensor out of 3D-printed PLA sections that interlock to form the sensor enclosure, with an aerodynamic taper at its front and rear. The sensor's center of gravity is between the forward cable and its quarter-length, stabilizing the system and ensuring that both wires remain taught during flight. Four fins near the rear assist its pitch- and yaw-stability.

The team decided to tow the sensor with two separate tow cables to maximize its stability and maintain a level attitude at low speeds. These cords have a 0.15 in. diameter and carry three signal wires that are covered in flexible black insulation. Three-position clipping connectors secure the cable to the sensor without interrupting the signal.

Within the sensor, three pulse-width modulation (PWM) switches-- each soldered to a wire-- controls the current passing from the sensor's onboard battery to light-emitting diodes (LED) secured to the bottom of the sensor. The team wrote a pilot-controllable program onto the deployment mechanism transmitter that creates a blinking pattern. While activated, the switches allow one LED to turn on for 1 s., one at a time in a repetitive, sequential order. **Figure 5.3.j** illustrates a side, external view; **Figure 5.3.k** shows an internal view of the sensor and its electronic components.

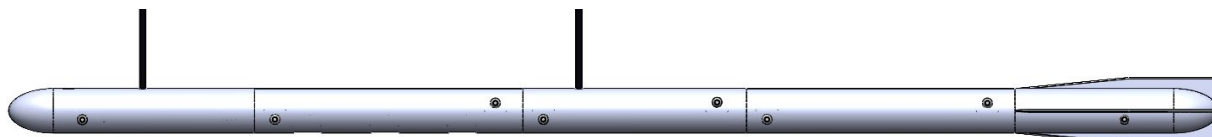


Figure 5.3.j: Side, external view of the sensor.

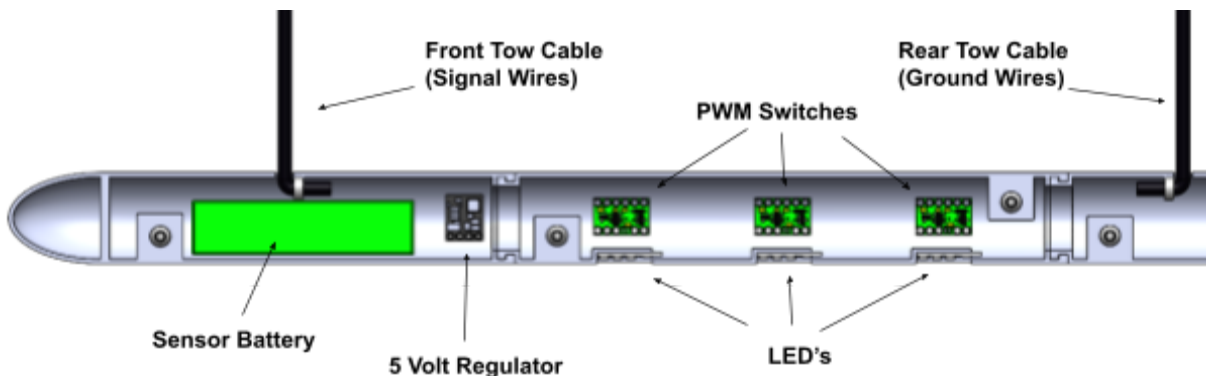


Figure 5.3.k · Internal layout of the sensor and its electronic components.

Shipping containers :: Basswood panels, $\frac{1}{8}$ in. thick and adhered together with wood glue, compose the walls of the sensor-shipping container. A sliding panel, fixed into place by an adhesive tape, encloses the sensor. Rigid foam blocks, of equal dimension to the sensor-shipping container, make up the others; the team bored holes into the foam, adding denser material to match the sensor's weight. **Figures 5.3.l** and **5.3.m** show the sensor's placement within a container.



Figure 5.3.l · View of the sensor within the shipping container, with a transparent side panel.

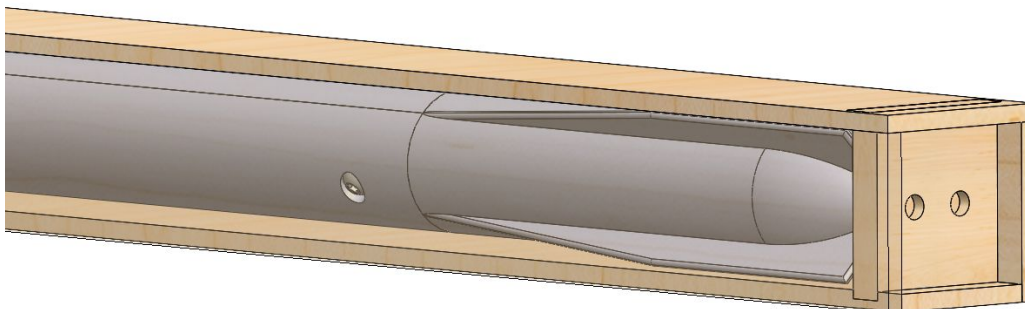


Figure 5.3.m · View of the shipping container's sliding panel, with a transparent side panel.

Deployment mechanism :: The aircraft's deployment mechanism, as shown in **Figures 5.3.n** and **5.3.o**, consists of two 3D-printed PLA spools mounted on a rotary shaft. They're coupled to a stepper motor that rotates the whole assembly. Two 3D-printed PLA bulkheads act as mounting points for the side panels, spools, and stepper motors. A battery and receiver are also attached to the mechanism, secured between the spools.



Tow cables with signal wires, each 270 *in.* long, are wound around the spools when stowed; they're connected to the receiver to provide communication to the sensor. The sensor-side ends of these cables are passed through guide sleds. A timing belt-- driven by a second stepper motor-- are attached to them, allowing the sleds to neatly and reliably guide the cable to the spools and preventing the wires from being improperly rewound while retracting. The deployment mechanism is attached to the fuselage using bolts embedded in the top panel of the mechanism. The bolts pass through holes in the fuselage and are tightened down with wing nuts on the top surface of the fuselage.

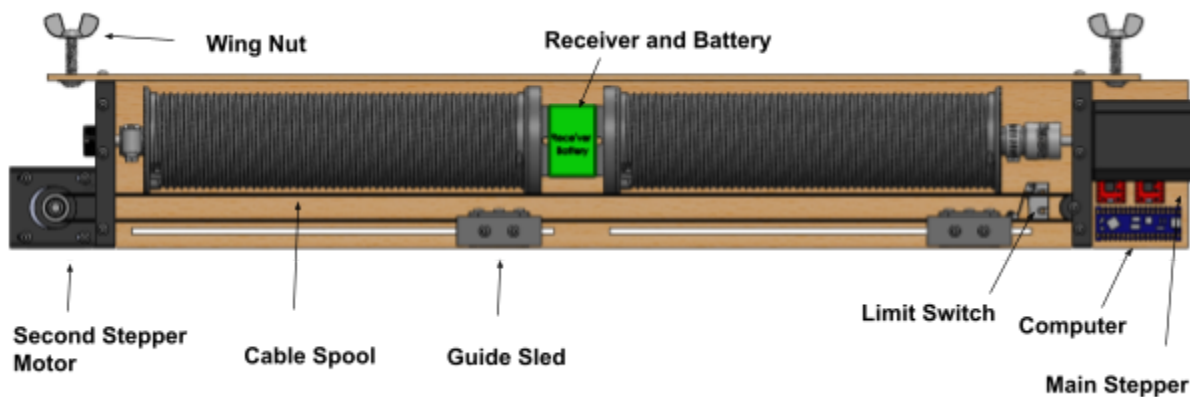


Figure 5.3.n · Side view of the deployment mechanism, with a side panel removed to view the internal system.



Figure 5.3.o · Isometric view of the deployment mechanism, with a side panel removed to view the internal system.



A limit switch, placed in line with the forward guide sled, as shown in **Figure 5.3.n**, calibrates the system. When the guide sled contacts this switch after the initialization of the hardware, the onboard computer recognizes that the system is in the fully retracted position.

The pilot controller's three-position switch controls the deployment mechanism. When it's set to the lowering position, the onboard computer activates the motors for a predetermined number of steps to deploy the sensor. When signaled to retract, the computer flips the motor's direction until the sensor reaches the initial position. The pilot can move the switch at any point during these processes into the neutral position to pause the motion.

Avionics :: The team selected the FrSky S8R receiver, in conjunction with the FrSky X9D+ transmitter, to utilize its special telemetry port's live display and logging functions. To drive the motors, the team chose 32-bit FrSky Neuron 80 ESCs for its ability to measure current, ESC temperature, motor speed, power consumption, and voltage; fast throttle response; and smooth motor cogging. They also daisy-chained a FrSky pitot-tube into the S.Port to record the aircraft's speed.

The team chose KST X08N as tail V5 servomotors and X10-710 as wing servomotors because of their wide voltage ranges and compact aluminum construction. At 8.4 V, the X08N produces 39 oz.-in. of torque; the X10-710 produces 104.16 oz.-in. of torque.

Their avionic system runs on a higher voltage (8.4 V). This reduces the possibility that the carbon fiber wing's construction causes a receiver brownout, improves its connection strength, and increases the servomotors' torque output.





5.4 - Weight and balance :: Figure 5.4.1 includes the plane's component weights and positions from the motor firewalls toward the aircraft's rear (+X-direction) and below the thrust line (+Z-direction), along with the resultant weight and center of gravity positions for all configurations. Since the aircraft is symmetrical about the centerline, the distance along the Y-direction can be ignored.

Component and count		Case	Weight	X-distance	Z-distance
Battery	x2	M-1	46.0 oz.	2.0 in.	2.0 in.
		M-2	46.0 oz.	-3.0 in.	2.0 in.
		M-3	46.0 oz.	-10.0 in.	2.0 in.
Empennage	x1	ALL	5.0 oz.	38.0 in.	-5.0 in.
ESC	x2	ALL	4.0 oz.	16.0 in.	1.0 in.
Fuselage	x1	ALL	10.1 oz.	3.0 in.	2.0 in.
Landing gear	x1	ALL	3.4 oz.	-2.0 in.	4.0 in.
Motor	x2	ALL	20.7 oz.	0.0 in.	0.0 in.
Receiver	x1	ALL	0.5 oz.	15.0 in.	1.0 in.
Wing	x1	ALL	17.7 oz.	2.0 in.	0.0 in.
Payload container	x10	M-2	121.6 oz.	9.0 in.	3.0 in.
Deployment mechanism	x1	M-2	28.0 oz.	-3.0 in.	2.0 in.
		M-3	28.0 oz.	30.0 in.	2.0 in.
Sensor	x1	M-3	11.2 oz.	9.0 in.	3.0 in.
Total		M-1	107.3 oz.	3.8 in.	1.8 in.
		M-2	256.9 oz.	4.6 in.	1.3 in.
		M-3	146.5 oz.	5.2 in.	0.5 in.

Table 5.4.1 - Weight and balance. Distances in the X-direction are measured from the motor mounts; distances in the Z-direction are measured from the thrust line.



5.5 - Expected performance :: The team used the methodology and model described in § 4.5 to predict the aircraft's flight and mission performance, shown in **Tables 5.5.1** and **5.5.2**, respectively.

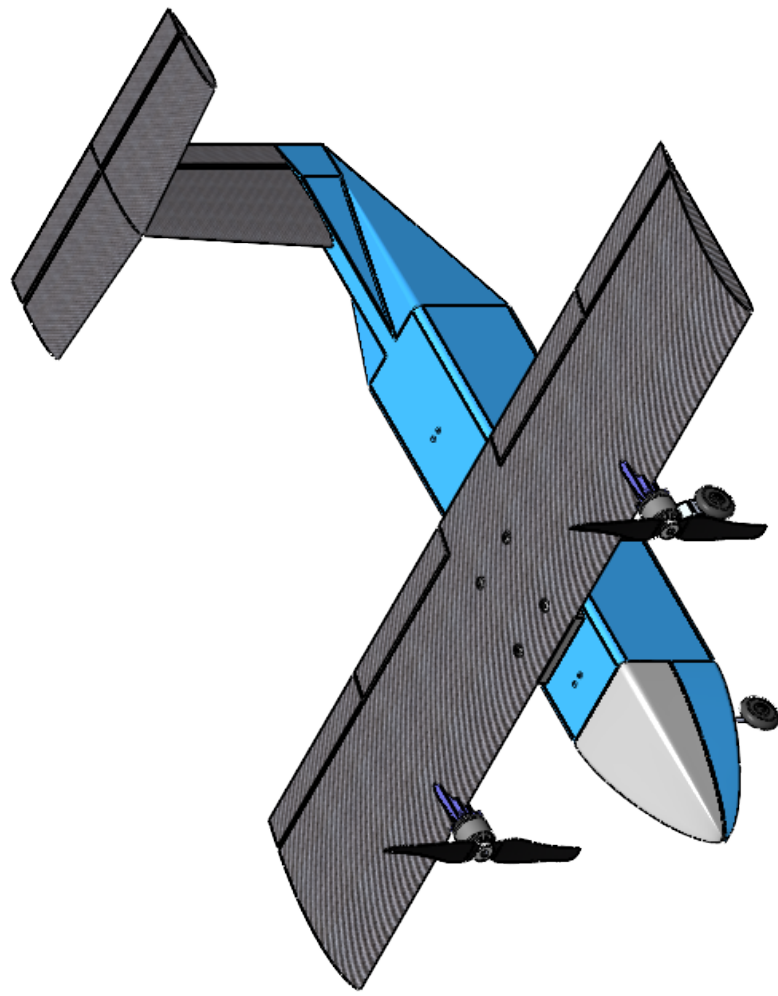
Parameter	M-1	M-2	M-3	
W_G	Takeoff weight	7.0 lb.	14.9 lb.	9.0 lb.
x_{TO}	Takeoff distance	35.0 ft.	118.0 ft.	58.0 ft.
I_{TO}	Takeoff power draw	83.0 A	128.0 A	89.0 A
v_{CR}	Cruise speed	70.4 ft./s.	104.1 ft./s.	80.7 ft./s.
I_{CR}	Cruise power draw	18.4 A	22.7 A	21.7 A
T_{TF}	Endurance	13.7 min.	11.1 min.	11.9 min.
v_{SL}	Steady-level speed	65.4 ft./s.	95.7 ft./s.	74.2 ft./s.
D_{SL}	Steady-level drag	0.9 lbf.	1.6 lbf.	1.2 lbf.
v_{BT}	Banked-turn speed	80.0 ft./s.	117.2 ft./s.	90.8 ft./s.
D_{BT}	Banked-turn drag	1.4 lbf.	2.8 lbf.	1.7 lbf.
	Per-lap energy usage	161.1 mAh	138.0 mAh	144.5 mAh

Table 5.5.1 - Model-generated estimated flight performance parameters.

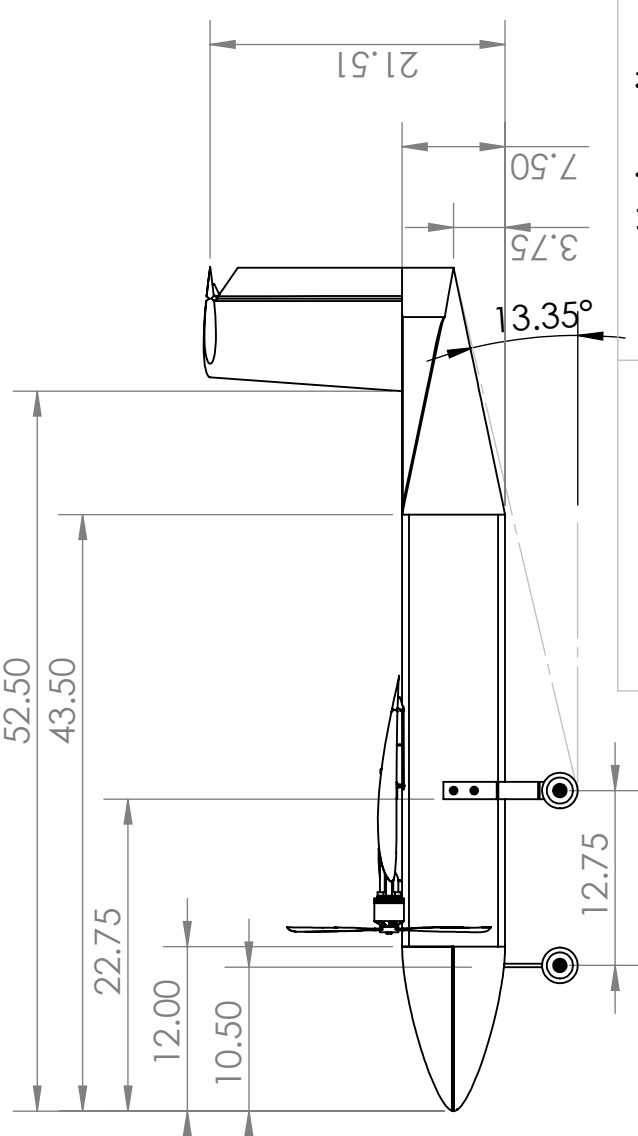
Parameter	M-1	M-2	M-3	
T	Per-lap time	31.5 s.	21.9 s.	27.9 s.
x_{TO}	Total time	94.5 s.	65.7 s.	600.0 s.
nL	Number of laps	3	3	21
Sc	Projected mission score	1 of 1	1.1 of 2	2.9 of 3

Table 5.5.2 - Model-generated estimated mission performance parameters.

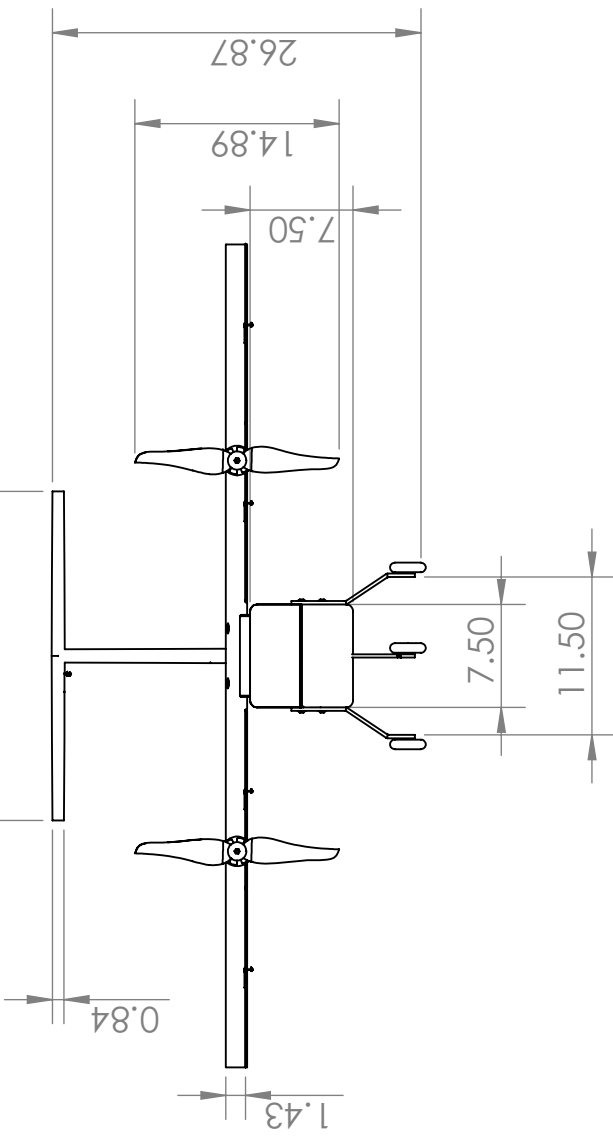
5.6 - Drawing package :: The next several pages contain the drawing package for UCSD DBF's 2020-21 fly-off aircraft.



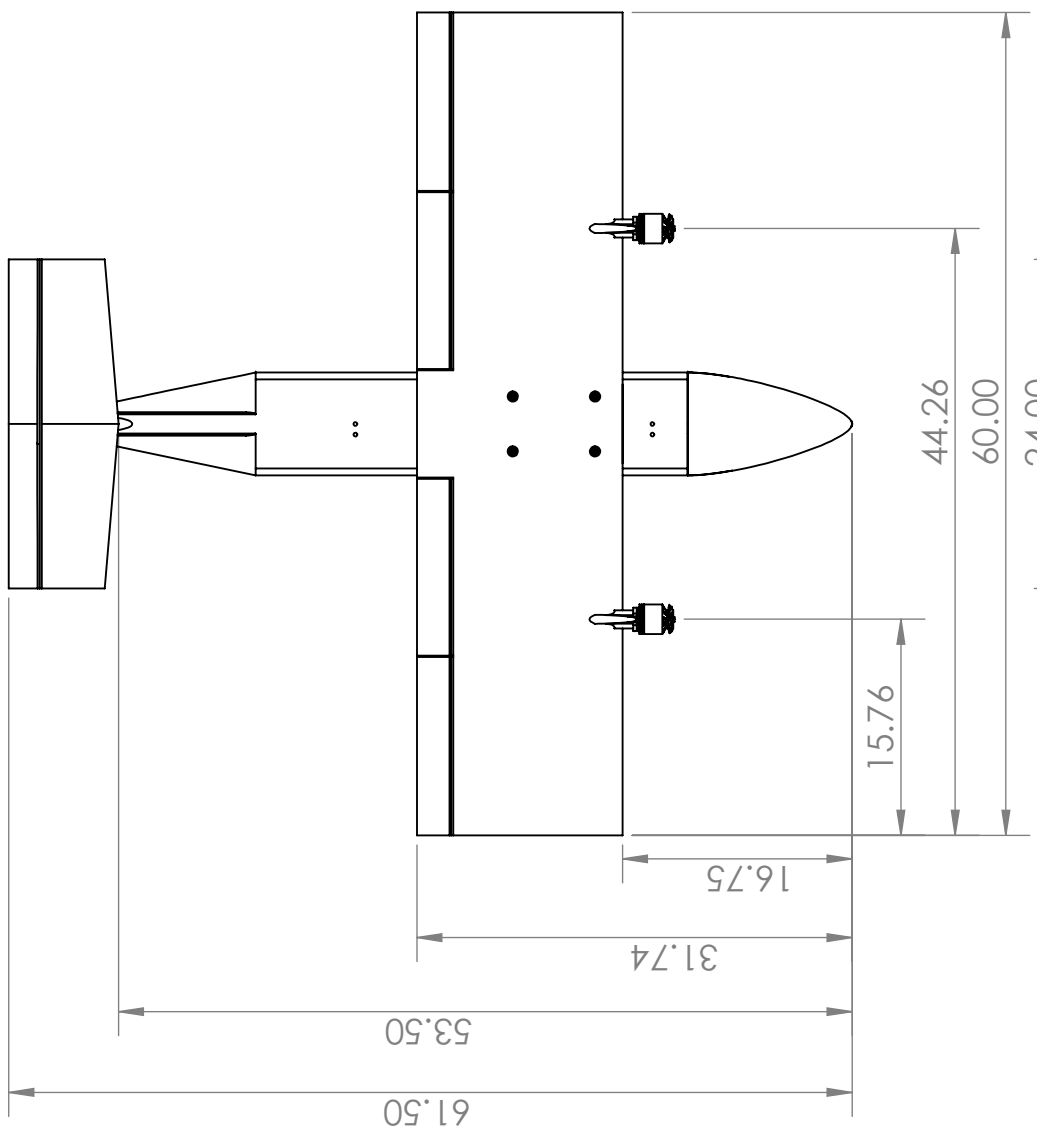
2



1



2



University of California
San Diego

TLAR

3 View

Drawn by:
Jacob Gruber

Drawn by:
Jacob Gruber

Drawn by:
Jacob Gruber

02/19/2021

02/19/2021

02/19/2021

University of California
San Diego

TLAR

3 View

Drawn by:
Jacob Gruber

Drawn by:
Jacob Gruber

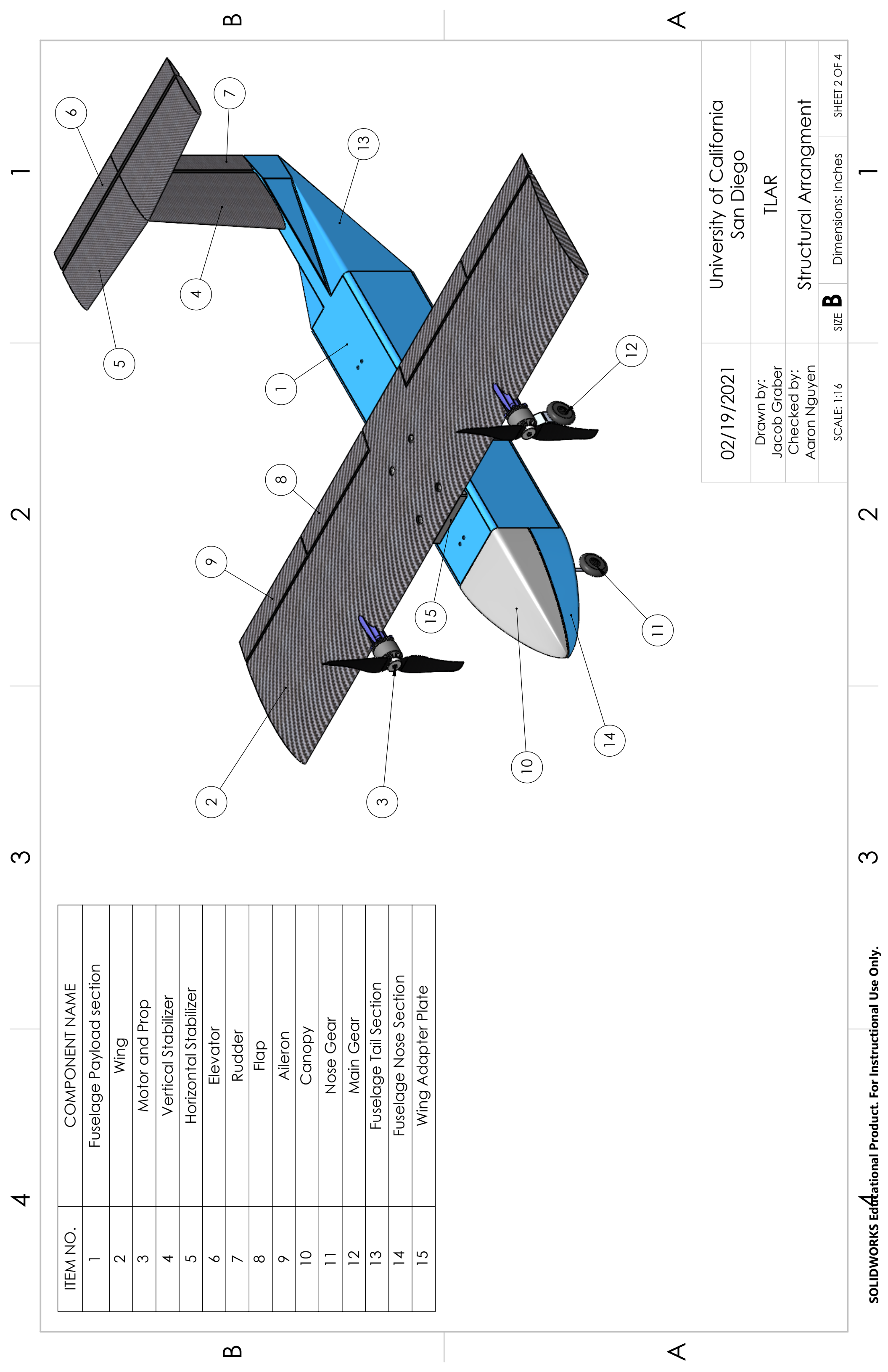
Drawn by:
Jacob Gruber

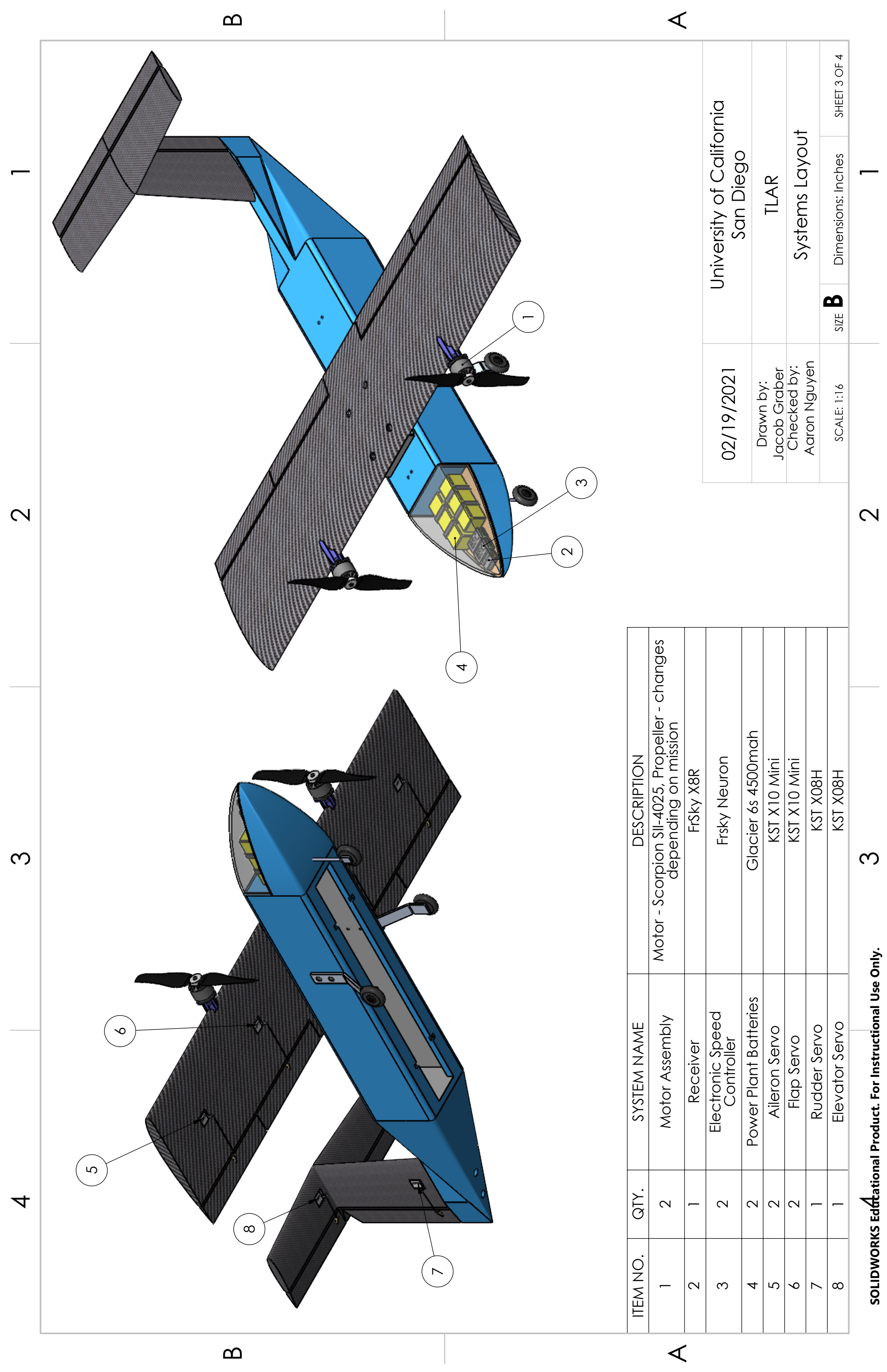
02/19/2021

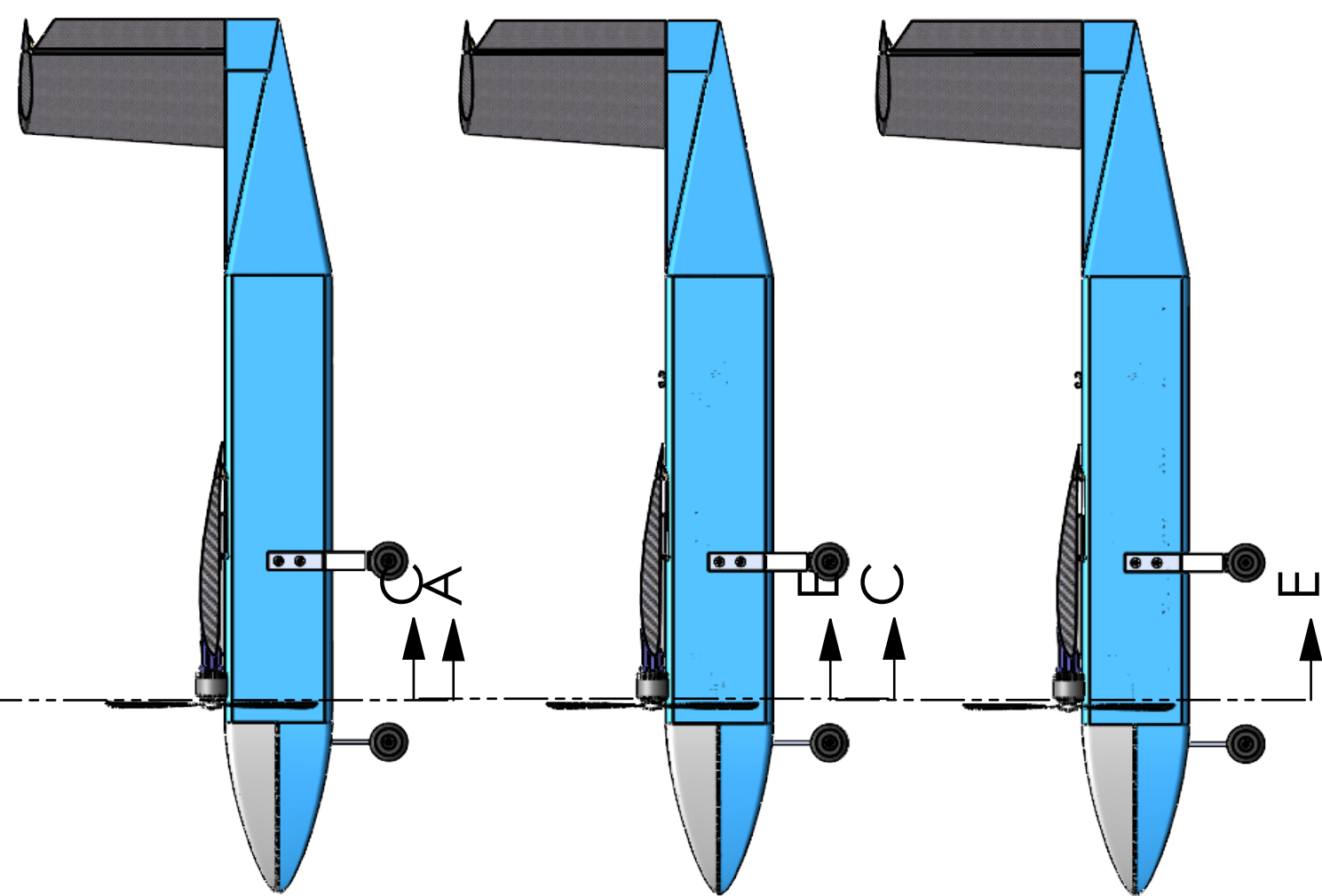
02/19/2021

02/19/2021

SOLIDWORKS Educational Product. For Instructional Use Only.







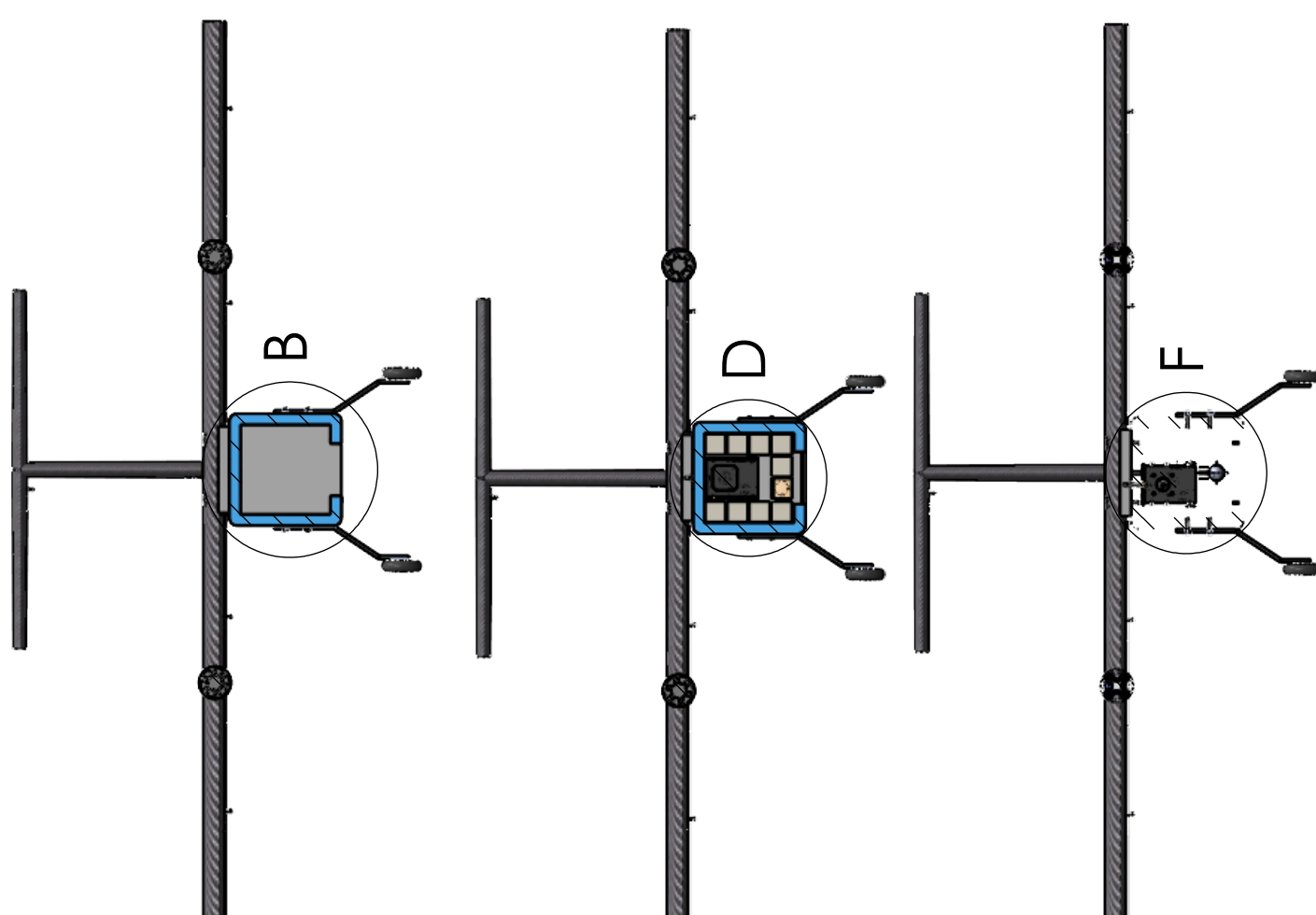
University of California
San Diego

Payload Accommodation TLAR

B Dimensionless Number SURET 1 OF 1

SCAIE: 1:31

2

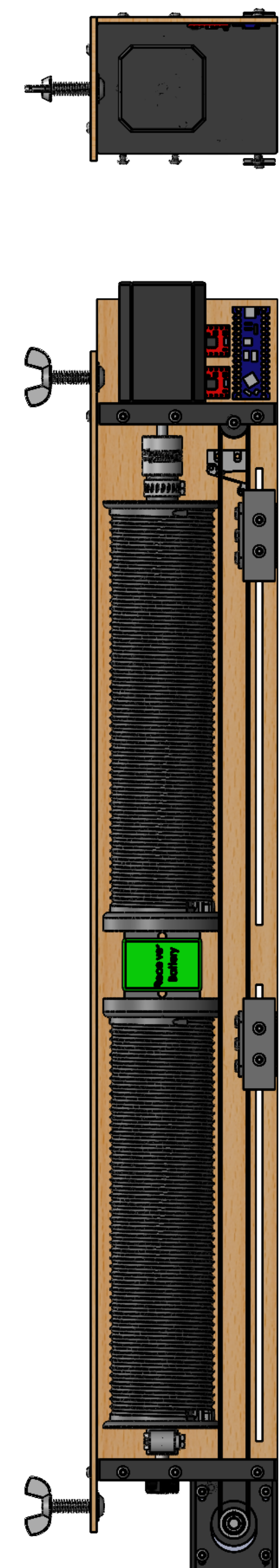


4

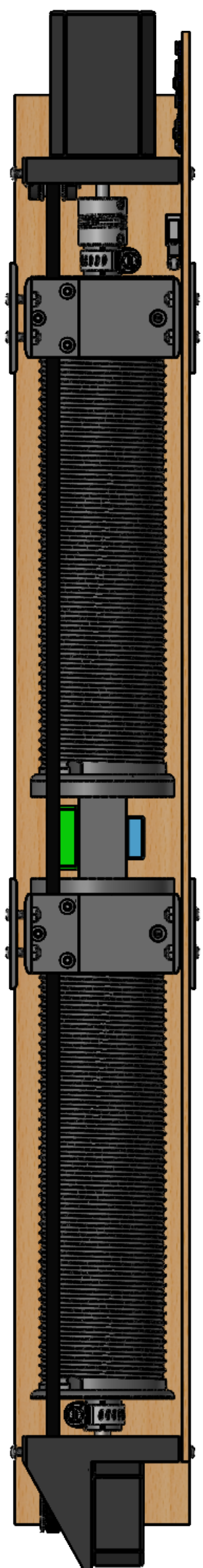
Mission 1 Config.

Mission 2 Config.

Mission 3 Config.



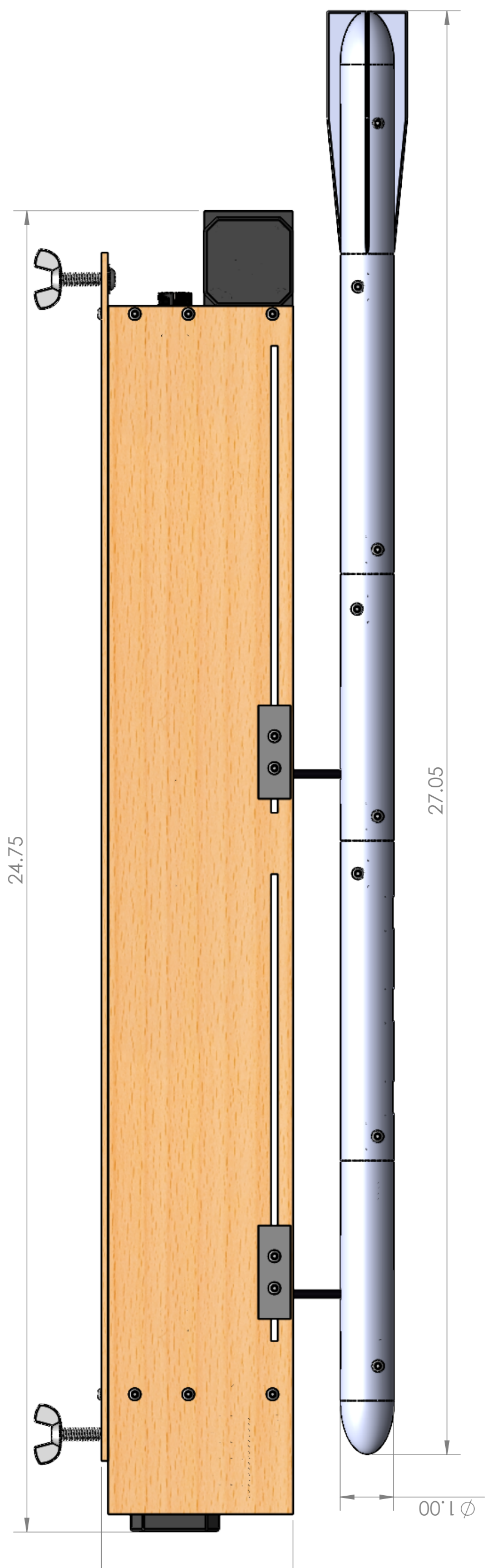
B



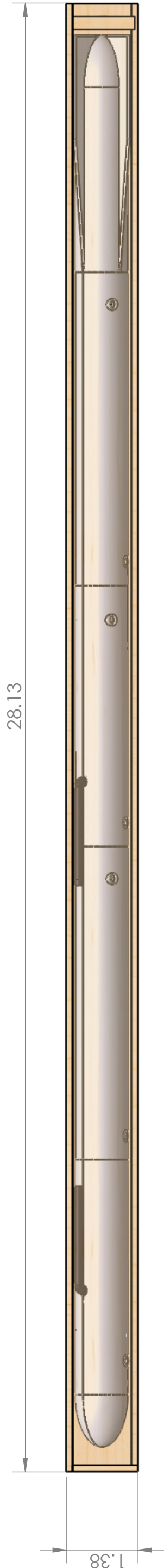
A

02/19/2021	University of California San Diego	Dimensions: Inches	SHEET 1 OF 1
Drawn by: Jacob Gruber	Checked by: Aaron Nguyen	SIZE B	TLAR
SCALE: 1:8	Deployment Mechanism	Dimensions: Inches	SHEET 1 OF 1

Mission 3 Deployment Mechanisms and Sensor Configuration



Sensor in Shipping Container



University of California
San Diego

TLAR
Deployment Mechanism, Sensor,
Shipping Container

Dimensions: Inches
SCALE: 1:8
SIZE B
SHEET 1 OF 1

§ 6

Manufacturing plan

The following section evaluates several manufacturing methods and materials to build the aircraft. It also describes the chosen assembly methods and outlines the team's manufacturing timeline.

6.1 - Investigation of manufacturing processes :: To find a production method that meets the design criteria of a high-performance and reliable aircraft and suits their current manufacturing capabilities, UCSD DBF investigated multiple methods of production.

Methods	Advantages	Disadvantages
3D-printing	<ul style="list-style-type: none">- Low cost- Capable of making very complex parts- Parts can be quickly printed	<ul style="list-style-type: none">- Relatively fragile- Parts size restricted to printer size
Balsa wood	<ul style="list-style-type: none">- Low cost- Parts can be made expediently	<ul style="list-style-type: none">- Requires complex digital modeling to design
Carbon fiber composites	<ul style="list-style-type: none">- High stiffness to weight ratio- Lightweight	<ul style="list-style-type: none">- Expensive- Time-consuming layup process- Blocks certain frequencies of radio signals
Fiberglass composites	<ul style="list-style-type: none">- Does not block radio frequencies- High strength to weight ratio	<ul style="list-style-type: none">- Comparatively weaker than carbon fiber- Shrinks and distorts when wetted with epoxy resin
Foam-core structures	<ul style="list-style-type: none">- Can act as spacers to increase overall strength- Allows for quick prototyping	<ul style="list-style-type: none">- Requires sanding for smooth surface
Hollow molded structures	<ul style="list-style-type: none">- Close resemblance to design profiles- Can be created using various materials	<ul style="list-style-type: none">- Time-consuming to fabricate the mold

Table 6.1.1 - Production methods in consideration.

6.2 - Assembly method selection :: After assessing the production methods listed in **Table 6.1.1**, the team optimized for assembly methods of specific components for the aircraft.

Fuselage :: While composite-based constructions provide weight reductions and strength improvements, the ease of building of foam board structures allow the team to prototype multiple fuselage designs. Foam board is also inexpensive and can be easily repaired or replaced if significant damage occurs. For its assembly, the team cut and joined $\frac{3}{4}$ in. thick polystyrene sheets to create the structure of the fuselage. They applied fiberglass to the exterior of the fuselage to add strength.



Wing :: The team used a hot-wire to cut acrylic templates in the shape of the airfoil to manufacture the wing. Using a hand router, channels were cut into the foam core and servo cables were laid inside to avoid running wires over the finished wing. Another channel was cut and a carbon fiber spar was placed between the two halves of the foam cores for added rigidity. Carbon fiber sheets were then placed on nonstick mylar sheets and saturated with epoxy resin. For weight reduction, any excess resin was blotted with paper towels. To create durable joints for control surfaces, kevlar strips were placed underneath the carbon fiber which would be later cut to make moveable flaps and ailerons. For structural integrity, extra carbon fiber was also added to the leading edge of the wing. Then the foam core was inserted between the carbon fiber covered mylar sheets and vacuum bagged.

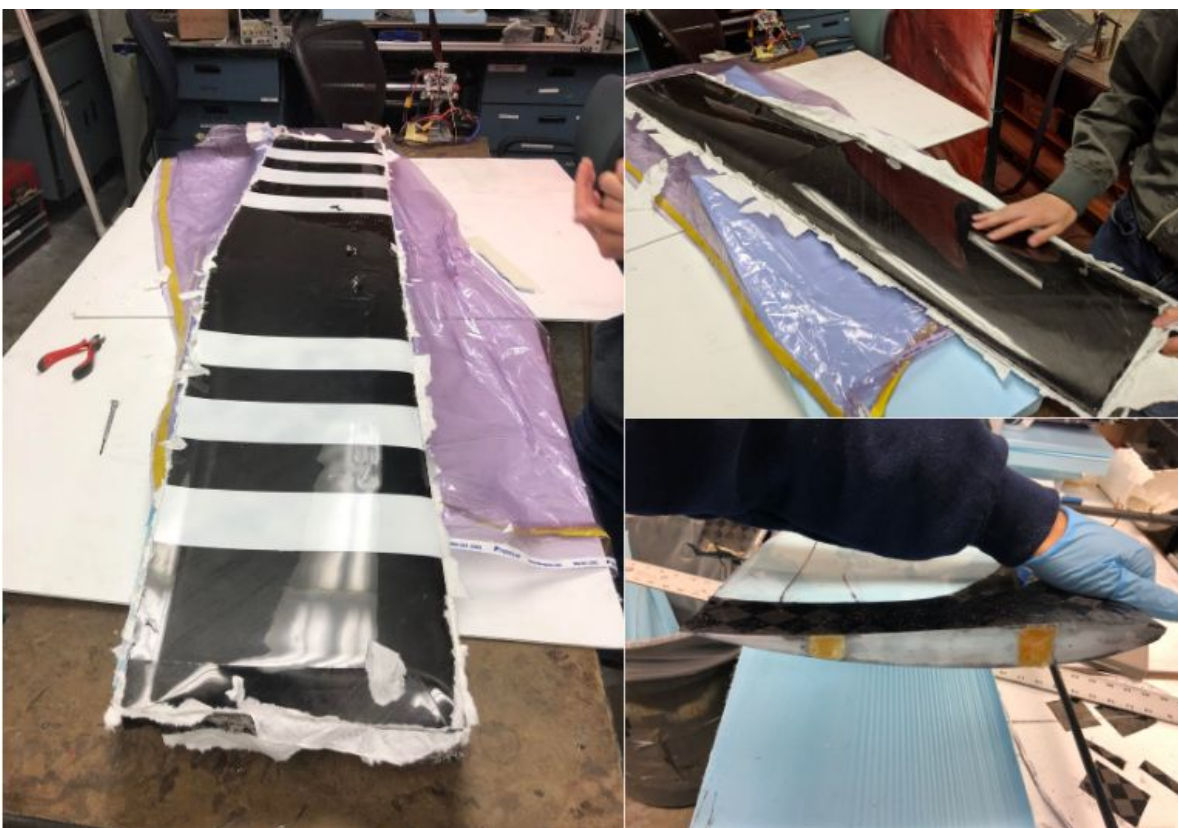


Figure 6.2.a Construction of the wing.

Tail :: The tail was constructed using the same composite layup process as the wing. Carbon fiber was overlaid over a foam core cut by a hot wire and vacuum bagged. In order to withstand the aerodynamic loadings, the T-shaped tail section has two all-threaded rods inserted into it, with part of the rods extending from the surface of the empennage. These were then fastened with nuts to the fuselage. Two 3-D printed L brackets were glued to the vertical and horizontal stabilizers to strengthen the joining of the two, and thin kevlar strings were tied at both ends of the vertical stabilizer to the fastened rods on the fuselage for tensioning and keeping the empennage intact. All control surfaces were covered with gap-covering tape and servos were covered with aerodynamics shrouds.



Figure 6.2.b · Detailed view of the tail assembly (left) and servomotor installation (right), with the aerodynamic shroud removed.

6.3 · Manufacturing timeline :: In light of the COVID-19 pandemic, subsequent public health restrictions restricted the team's access to their workshop. Their prototype design could not be fabricated; thus, they could only fabricate one aircraft for the 2020-21 contest season. The sole prototype constructed during this competition season served both as a testing and competition plane.

MONTH OF	9/2020	10/2020	11/2020	12/2020	1/2021	2/2021	3/2021	4/2021																						
WEEK OF	21	28	5	12	19	26	2	9	16	23	30	7	14	21	28	4	11	18	25	1	8	15	22	1	8	15	22	29	5	12
FABRICATION	PLANE GENERATION: PROTOTYPE												PLANE GENERATION: COMPETITION																	
Wing and Tail			#1										#3																	
Fuselage																														
Sensor/Container																														
Towing Mechanism																														
Landing Gear																														
Electronics																														
TESTING	PLANE GENERATION: PROTOTYPE												PLANE GENERATION: COMPETITION																	
Static Propulsion Testing																														
Structural Testing																														
Sensor/Container																														
Towing Mechanism																														
Electronics																														
Flight Test														#2														#4		

Milestones: #1 Prototype Design Freeze #2 Prototype Plane Complete #3 Competition Design Freeze #4 Competition Plane Complete

Figure 6.3.1 · Manufacturing timeline.



§ 7

Testing plan

To gather flight data and optimize the performance of its competition aircraft, UCSD DBF created and executed a plan to test the aircraft's sub-systems. This section discusses the team's comprehensive testing process extensively.

7.1: Aircraft and subsystem testing plan :: The team has planned two test flight periods throughout the 2021 competition season; the test schedule is shown in **Figure 7.1.a**. With the limited techniques and tools available to them, the team conducted several tests on the aircraft's propulsion set-up, structural components, and other subsystems.

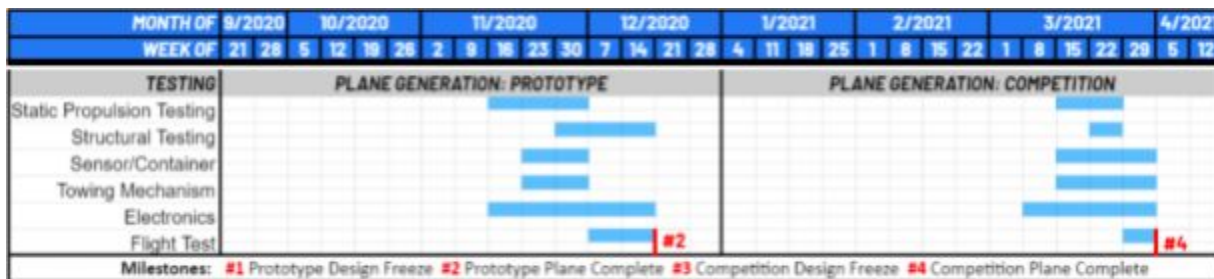


Figure 7.1.a: Testing schedule and timeline.

Static propulsion testing :: To verify that it performed similarly to their theoretical calculations, the team used an RC Benchmark dynamometer to measure the current, motor speed, static thrust, and voltage of the selected propulsion system (a 420 Kv Scorpion SII-4025 with three different propellers) across various throttle settings.

Structural testing :: The team performed several tests before flight to validate the structural integrity of their aircraft. They tested the carbon fiber spar's ability to support the aircraft's full weight and placed weights on the root of the wings to simulate the maximum loading conditions from earlier calculations. After completing the prototype, the team conducted two wingtip tests-- while the aircraft was unloaded and fully-loaded-- to test the safety of its fuselage and wing joints.

Container drop testing :: To ensure that it could survive a drop up to 10 in., the team subjected the sensor-carrying container to several drop tests of 20 in. on all six faces. They then inspected the sensor and the shipping container for damage.

Deployment mechanism testing :: To ensure the reliable deployment and retraction of the sensor while in flight, the team subjected the deployment mechanism to different test situations and potential operating conditions. They simulated the loads that the deployment mechanism may experience during high-g maneuver by testing its functionality with a heavier sensor-like object. They also held the system at extreme attitudes to determine its operational pitch and roll limits.



Throughout these tests, the team ensured that the sensor's connection did not break; thus, they routinely checked that the LEDs continued to operate.

7.2 - Flight testing plan :: In compliance with local and university COVID-19 guidelines, the team's pilot tested the aircraft near their household, away from the team's normal site in San Diego; during each session, the pilot communicated with the team and their advisors remotely.

The team created a progressive testing plan to ensure there was no unnecessary risk to the airframe and started its maiden flight without any additional payload. Such a strategy also allowed the team to find and fix unforeseen problems and other instabilities. If they found any, the team consulted flight and the ESC-obtained telemetry data, made the changes necessary to remediate these issues, and, as they saw fit, conducted additional test flights.

Pre-flight checklists :: Before flying the aircraft, the team must've satisfied the conditions presented in **Figure 7.2.a** and obtained the endorsements of the personnel listed in **Figure 7.2.b**.

Preflight Checklist			
Propulsions		Payload	
Propeller Direction?	<input type="checkbox"/>	Weight verified?	<input type="checkbox"/>
Propeller Secured?	<input type="checkbox"/>	Payload Secure?	<input type="checkbox"/>
Aircraft			
Batteries Charged?	<input type="checkbox"/>	CG Verified?	<input type="checkbox"/>
Battery Voltages +/- .3V?	<input type="checkbox"/>	Wing bolts tight?	<input type="checkbox"/>
Reciever Pack Charged?	<input type="checkbox"/>	Hatches closed?	<input type="checkbox"/>
Reciever On?	<input type="checkbox"/>	Landing Gear Tight?	<input type="checkbox"/>
Connection Secured	<input type="checkbox"/>		

Figure 7.2.a - First pre-flight checklist.

Final Checklist			
Controls		Signatures	
Reciever Connection?	<input type="checkbox"/>	Pilot	_____
Control Surfaces Responsive?	<input type="checkbox"/>	Faculty Advisor	_____
Telemetry Software On?	<input type="checkbox"/>	Project Manager	_____
Visual Inspection?	<input type="checkbox"/>	Date	_____

Figure 7.2.b - Final pre-flight checklist. The team should obtain the signatures of the pilot, faculty advisor, and project manager before proceeding.



Flight tests :: After the prototype's completion on 20 January 2021, the team pilot conducted nine test flights over two sessions; **Table 7.2.1** describes each test and the environment in which they conducted them.

Date and location	Air temperature	Wind speed	Flight number	Flight designation	Simulated mission	Payload weight
21 January 2021 San Ramon, California	58 °F	4 ft./s.	1	1-MF	M-1	0.0 lb.
			2	1-M1	M-1	0.0 lb.
			3	2-MF	M-2	1.9 lb.
			4	2-M1	M-2	3.8 lb.
			5	2-M2	M-2	5.6 lb.
			6	2-M3	M-2	7.5 lb.
4 February 2021 San Ramon, California	62 °F	17 ft./s.	7	3-MF	M-3	0.1 lb.
			8	3-M1	M-3	0.5 lb.
			9	3-M2	M-3	1.0 lb.

Table 7.2.1 · List of test flights.



§ 8

Testing plan

UCSD DBF conducted its first test after completing the aircraft prototype on the week of 20 January 2021. The following section documents the results of the tests described in § 7.

8.1 Aircraft and sub-system performance :: The team compiled the results of the component-wise tests, and observed their performance in actual flight.

Propulsion tests :: The team's test stand data, which gathers the propulsion system's static thrust and various electrical quantities, are documented in **Table 8.1.1**.

Propeller	Maximum current	Maximum power	Maximum speed	Voltage
11 in. × 6 in.	43.2 A	1058 W	96 ft./s.	24.5 V
12 in. × 10 in. -E	38.4 A	940 W	132 ft./s.	24.4 V
11 in. × 7 in. -E	40.6 A	1003 W	106 ft./s.	24.7 V

Table 8.1.1 · Static motor test results.

The Scorpion motors are a good solution for the team's performance goals. It provided enough thrust and operated efficiently while towing a sensor and lifting large payloads. The team encountered several easily remedied issues; unbalanced propellers created excess vibrations at certain throttle ranges and an initially nose-heavy center of gravity placement. The plane drew 12 A of current per motor while cruising-- a success, given the propulsion setup and size of the aircraft.

The team expected its batteries to drain quickly during takeoff-- the most intensive period of flight. This was quite evident from the team's telemetry data; takeoffs drew 60 A and used about 35 mAh from the battery pack. Overall, however, the tests confirmed the team's propulsion choices. The LiPo packs supplied enough current, did not overheat, nor excessively sag under loads in-flight.

Structural tests :: After conducting tests at maximum load, the team inspected the spar and wing thoroughly for any visual signs of bending, yielding, or damage; there were none. Further tests, such as wingtip testing, in **Figure 8.1.a**, were successful.



Figure 8.1.b · Wingtip test prior to first flight.

The team tested the landing gear to support the entire weight of the aircraft both statically and under high impact. It was found during the initial testing that the front landing gear was too short and made the aircraft sit at near-zero angles of attack. This resulted in failed takeoffs where the plane could not rotate during takeoffs. Modifications to the front landing gears, shown in **Figure 8.1.c**, were made to raise the nose up two inches.



Figure 8.1.c · Modification to the landing gear. An additional landing gear spring-steel wire was attached to the existing front landing gear to raise the nose of the aircraft.



8.2 - Flight performance :: The team compiled the aircraft's extreme speeds and cruising amperage from flight telemetry data. These values are recorded in **Figures 8.2.a** and **8.2.b**. **Figure 8.2.3** is a photograph of the aircraft during the test flight.

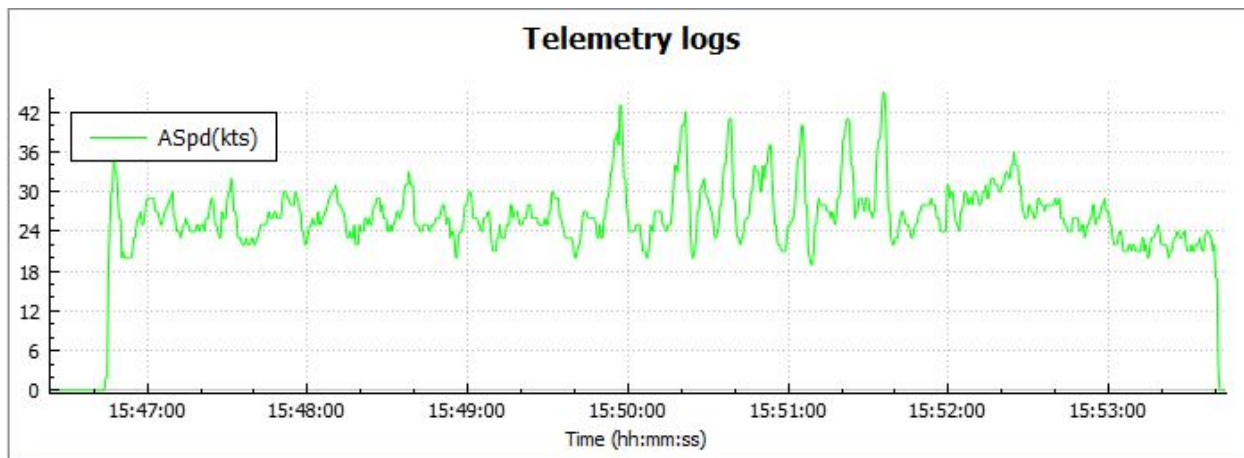


Figure 8.2.a · Airspeed, in *knots*, over time for the unloaded, M-1 test flight.

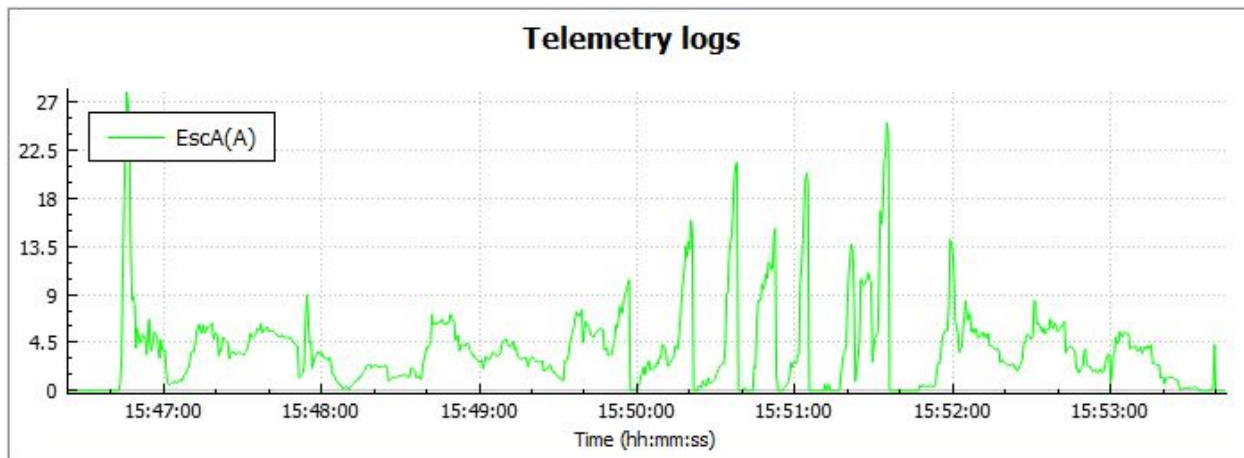


Figure 8.2.b · Current, in *A*, of a single ESC during the unloaded, M-1 test flight.

At 15:50:55, testing was performed to determine the maximum speed and amperage draw of the aircraft and can be seen in the peaks of the graph.

The above data was from the S.Port telemetry data collected during the first-mission test flight. The ESC data is recorded off of a single ESC. The peak amperage draw occurred at takeoff with 28 A drawn by one motor. For maximum speed tests, one single ESC drew 25 A at full throttle. The difference between takeoff and maximum speed can be explained by propeller unloading in the air.



Figure 8.2.c · Photo of the aircraft during the unloaded, M-1 test flight.

Table 8.2.1 summarizes the actual flight performance characteristics of the overall aircraft.

Propeller	Maximum speed	Minimum speed	Cruising current	Payload weight
M-1 tested	76.0 ft./s.	33.7 ft./s.	12.0 A	0.0 lb.
M-1 predicted	83.2 ft./s.	31.0 ft./s.	18.4 A	0.0 lb.
M-2 tested	86.5 ft./s.	51.0 ft./s.	19.0 A	7.0 lb.
M-2 predicted	122.0 ft./s.	43.0 ft./s.	22.7 A	8.0 lb.
M-2 tested	62.5 ft./s.	41.0 ft./s.	20.0 A	0.5 lb.
M-2 predicted	93.6 ft./s.	33.0 ft./s.	21.7 A	0.8 lb.

Table 8.2.1 · Tested and predicted flight performance parameters for each mission.

The flight data and testing showed that the plane underperformed on its expected cargo weight being carried and its top speed for the first- and third-mission. This could be because of a large amount of drag from the fuselage and the compounding effect it has in reducing the main wing's lift. The high stall speed also points to less lift being generated possibly due to the large fuselage blocking the wing.

Another flight characteristic that was observed was the unique stall characteristics at high angles of attack. The tail would "slide out" during a stall where the aircraft's heading would be different to the direction of motion. This unintentional knife edge condition, shown in **Figure 8.2.d**, could be correlated by the T-tail configuration and both flying style and gyro settings were adjusted to prevent this from happening again.

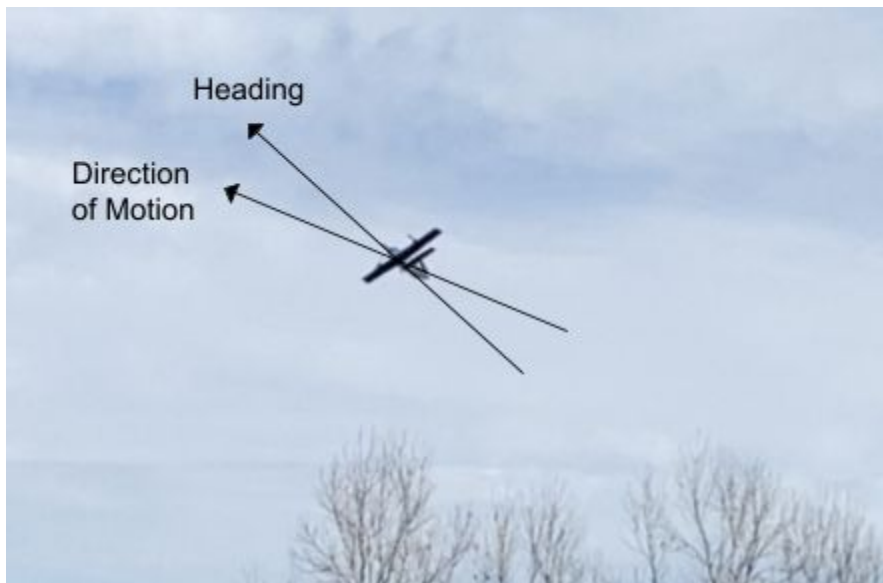


Figure 8.2.d · Unintentional knife edge that occurred during the second test flight.

8.3 · Future work :: The team plans to make several modifications to, and conduct several tests of, the final aircraft to improve aircraft performance. After analyzing the flight data performance, the team focused on where the airplane was underperforming and how to improve both the score and the flight characteristics of the plane. The fuselage and drag will be the focus for design revisions in order to find a more optimal fuselage design and improve performance of the aircraft. Also, excess weight will be slowly removed from the structure for better cargo carrying abilities. In the end, by the time of the video fly-off, UCSD DBF hopes to have a well-tested and refined aircraft that is optimized for both high performance and high reliability.





9

Bibliography

- [1] Hwang, J. T., Arnav V. J., and Tae H. H., "[Large-scale multidisciplinary design optimization—review and recommendations.](#)" AIAA, San Diego, CA, June 2019.
- [2] Bunge, R., "[Motor/propeller performance analysis and estimation.](#)" Stanford University, 8 April 2016.
- [3] "[Motors.](#)" Scorpion.
- [4] "[Performance data.](#)" Advanced Precision Composites.
- [5] Scholz, D., "[Drag Prediction.](#)" *Aircraft Design - an Open Educational Resource (OER) for Hamburg Open Online University (HOOU)*.
- [6] Hoerner, S. *Fluid-Dynamic Drag*, 2nd ed., DB Hoerner Fluid Dynamics, Albuquerque, NM, 1965.